MEMS-Based Millimeter Front-end for Automotive Radar Applications

by

Bahaedinne Jlassi

A thesis
presented to the University of Waterloo
in fulfillment of the
thesis requirement for the degree of
Master of Applied Science
in
Electrical and Computer Engineering

Waterloo, Ontario, Canada, 2018

AUTHOR'S DECLARATION

I hereby declare that I am the sole author of this thesis. This is a true copy of the thesis, including any required final revisions, as accepted by my examiners.

I understand that my thesis may be made electronically available to the public.

Abstract

Automotive front-end radars are key components in modern vehicles. They are used in automatic cruise control (ACC) for advanced drive-assistance and security functions, including collision-avoidance systems. Automotive safety is being studied intensively both in industry and academia. One of the most serious limitations of high performance radar are beam-forming network systems, due to the complexity and bulkiness arising from the additional circuitry and hardware needed to implement multiple functionalities into the systems. This limitation can, however, be minimized and made cost-effective by capitalizing on the numerous advantages of RF MEMS and WG technologies. To resolve this issue, the present study covers the characterization of SPST and SPNT RF-MEMS switches at 77 GHz, the investigation and fabrication of a Rotman lens at 77 GHz, and the development of the ground work for a 3D monolithically integrated BFN on a single silicon substrate.

Acknowledgements

First of all, I would like to thank my advisor, Raafat Mansour of the Electrical and Computer Department at the University of Waterloo. The door to Prof. Mansour's office was always open.

I would also like to thank the readers, my CIRFE-mates and the CIRFE manager, who participated in the formation of this thesis through their passion and valuable comments.

Finally, I must express my very profound gratitude to my parents and friends for providing me with unfailing support and continuous encouragement throughout my years of study, especially through the process of researching and writing this thesis. This accomplishment would not have been possible without you, so thank you.

Bahaedinne Jlassi.

Table of Contents

List of Figures

List of Tables

Chapter 1
Introduction

1.1 Motivation

Safe and collision-free travel has become a priority in today's society, given the loss of millions of lives every year through traffic accidents. Currently, automotive safety is studied intensively both in industry and in academia. By definition, the study of vehicle design and equipment to minimize the occurrence and consequences of accidents is "automotive safety". In fact, it has evolved from using typical means (e.g., seatbelts and airbags) to involve developed telematics systems known as automatic cruise control (ACC) for advanced drive-assistance and security function, including collision-avoidance systems. These systems can provide parking assistance, blind-spot detection, emergency braking, pre-crash detection, rear collision protection, headway alert, precise airbag activation, and forward collision warning, among other features.

Automotive radar (radio detection and ranging) sensing enables a 360° protection area surrounding the object under test. It is mainly ensured by using short-range radar (SRR) and long-range radar (LRR) in accordance with the range it covers. Typically, multiple short-range sensors are mounted around the automobile to detect objects at close range (0–20 m). However, single forward-processing radar could be sufficient for long-range detection (≈150 m). In both cases, these sensors and radars permit advanced driver-assistance and collision avoidance.

Based on the literature, radar front-end architecture includes three stages: a switching stage, an electronically scanned array (ESA) stage, and an antenna stage. In each compartment, switches, phased arrays (PA i.e., ESA) and antennas represent an opportunity for radio frequency microelectromechanical (RF MEMS) and micromachined waveguide (WG) technologies. Radars are a cornerstone in the development of intelligent transportation systems and have been studied and developed exhaustively during the last century. The challenges in designing a radar system are numerous, but the main ones are balancing the effectiveness of avoiding collisions versus the risk of false alarms, reducing the cost of the system for production purposes, and miniaturizing the system to make it more portable and less invasive. Therefore, the front-end system can be minimized and made cost-effective by utilizing the numerous advantages of RF MEMS and WG technologies.

The present thesis study presents the investigation, implementation and measurements of a fully-integrated Rotman lens operating in the approved band of 77 GHz in both RF-MEMS and

micromachined waveguide technologies. Integrated circuits employed in the transceiver designs enable the system to achieve high range resolution and to detect objects more effectively, thereby demonstrating its suitability for application in radar systems. This work suggests that advanced RF-MEMS and WG technologies could conceivably end the dominance of compound semiconductor technologies in automotive radar systems in the near future.

1.2 Main Objectives of the Dissertation

The principal objectives of the dissertation are as follows:

Objective 1	Characterization of SPST and SPNT RF-MEMS switches at 77 GHz, using new surface micromachining technology.
Objective 2	Investigation, demonstration and fabrication of a Rotman lens (RL) at 77 GHz.
Objective 3	Investigation of a 3D monolithically integrated BFN on a single silicon substrate consisting of MEMS-based SPNT switches, waveguide RL, and antenna array.

1.3 Outline of the Remaining Chapters

The outline of the remaining chapters is as follows. Chapter 2 presents a literature review of the radar front-end system, RF-MEMS switches, WG switches, ESA and antenna at 77 GHz, as well as previous integration attempts and previous proposed technologies and designs, etc. The third chapter introduces an initial theoretical and experimental study of RF-MEMS/WG 77GHz switches, a Rotman lens, and BFN-antenna at 77 GHz. Chapter 4 discusses the challenges and tasks involved in developing 3D monolithic structures. Finally, Chapter 5 summarizes the main concepts and ideas of the thesis and offers suggestions for possible future work.

Chapter 2
Literature Review

This chapter focuses on the basics of automotive radars through a literature review of popular automotive radar architectures, radar performance parameters, and several academic and industrial radars.

2.1 Automotive Radars

2.1.1 Introduction

Market research conducted by Strategy Analytics on automotive electronics has reported that safety technologies are the fastest growing applications in this field (Figure 2-1) and that Advanced Driver Assistance Systems (ADASs) are leading this growth. To assess the environment around the vehicle and warn the driver of any potentially hazardous situations, ADASs use long-range sensors (i.e., cameras, radars, and lidars).

The research shows that the volume demand for Electronic Control Units (ECUs) used in safety applications increased 12% per annum over the period 2006 to 2011 [4, 15].

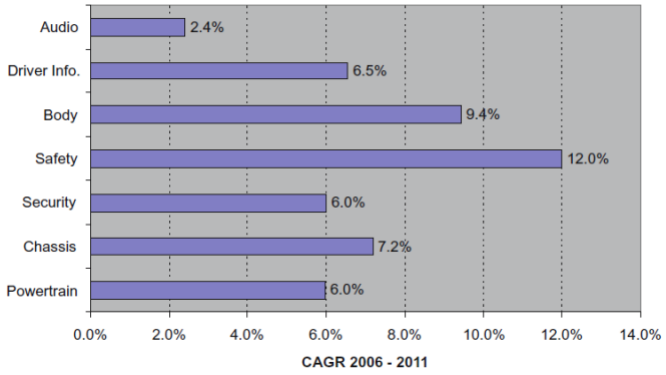

Figure 2-1 Automotive systems growth by application

Among the safety applications were collision warning systems that were successfully introduced in the USA in the 1990s. For example, when Greyhound installed more than 1600 radar systems in their buses, the result was the reduction of accidents by 21% from 1992 to 1993. Also, radar-based autonomous cruise control (ACC) systems were first introduced in the Mercedes S class series in 1999. To provide much better and higher braking forces for alerting a threatening situation, other safety

functions such as pre-crash sensing and collision mitigation which utilizes active break assist were also introduced [1, 2].

In terms of frequency allocation, automotive radars were regulated in the 1990s to use the 76 to 77 GHz band for Intelligent Transport Services (ITS) in Europe, North America and Japan. In 2002, the Federal Communications Commission (FCC) allocated the band 22 to 29 GHz for the UWB short-range radar (SRR) systems GHz.

Due to the opposition of the lower frequency band (22 to 29 GHz) by the telecom industry and various Earth observation institutions, the development of UWB SRR systems was shifted to the use of only the upper band (76 to 81 GHz) [2, 9, 35].

2.1.2 Automotive Radar Fundamentals

The term "radar" is an abbreviation of "radio detection and ranging" (radar). It is traditionally the most common tracking sensor used for the detection and location of objects. Radar operates by transmitting a particular type of waveform and detecting the nature of the signals reflected back from objects. The technology is used to sense the angle, range and velocity of moving objects in a specific area. Radar was intensively utilized in military applications for many decades before becoming common in civil applications. For example, radars have been introduced in air traffic management (ATM), fire control, ground-penetrating radar (GPR), weather forecasting, naval applications, and lately in automotive autonomous cruise control (ACC) systems. Because the focus of this thesis is automotive radars, we will concentrate on concepts related to the specific field of automotive radar systems [21].

Automotive radar sensors ensure the safety of the vehicle from all sides (Figure 2-1). The typical system is constituted from several SRR sensors to detect objects at close range (0–40 m) and one forward-looking sensor for long-range detection (≈150 m).

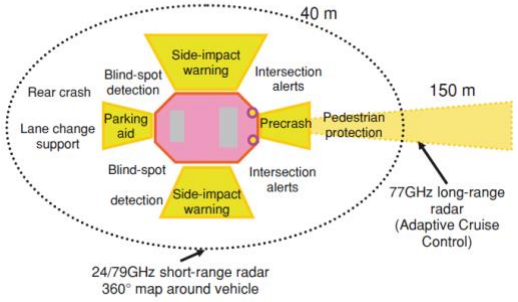

Figure 2-2 Automotive radar sensors

Given their applicability, radar sensors have several advantages over other sensing technologies such as video, lidar and ultrasound. These advantages include the quick measurement of range, tolerance to weather conditions, ease of installation in typical automotive fascia, and reduced cost [5, 8].

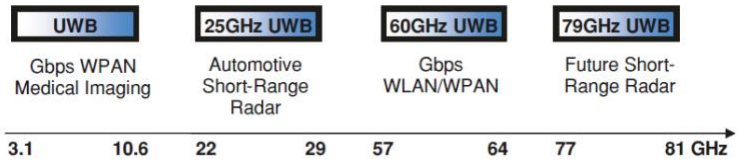

Figure 2-3 Automotive radar range

Radar sensors provide the measurements of the range (r), range rate (r'), azimuth angle (ϕ), and elevation angle, as illustrated in Figure 2-3. The radar sensor emits an electro-magnetic radiation to detect targets through the analysis of the reflected signal. The emission and reception of those waves are usually performed by the same antenna, with the sensor switching between the two modes [33].

The antenna design dictates the shape of the radiation pattern. In automotive radars, the antenna is designed so that the main lobe has a conical shape. The beam width is typically from 1 to 4 degrees in both the azimuth and the elevation direction. The object position angles are calculated through either mechanical sweeps of the antenna over a range or electronically switching between different emission angles. Those techniques made the total field of view (FOV) (see Figure 2-4 for an example) to be normally 10 to 15 degrees. Most existing automotive radars provide only the azimuth measurements.

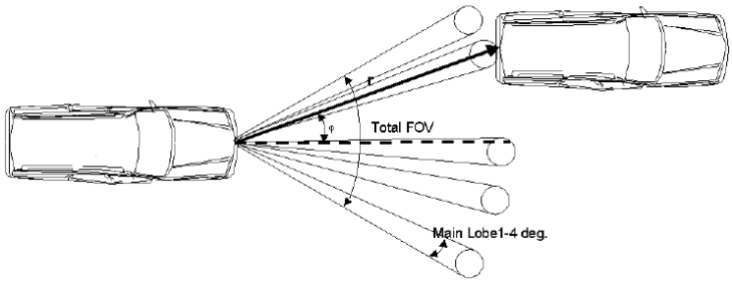

Figure 2-4 Measurements provided by radar sensor

2.1.3 Automotive Radar Architecture

Several classifications of automotive radar systems are discussed in the literature. They are typically categorized by the architecture and propagation window. Because the propagation window was already discussed in the previous section (24 GHz, 77 GHz, etc.), we will discuss here the different architectures

of automotive radars. Automotive radars can be classified based on the range (short or long) of the transmission or on the waveform (continuous or pulsed).

2.1.3.1 Range-based Classification

In this classification, the two main categories are short-range radar (SRR) and long-range radar (LRR).

2.1.3.1.1 Short-range Radar (SRR)

SRR is used to monitor areas within a 30 m range at an angle of 80°, whereas LRR is used to monitor areas at a distance of up to 150 m (see Figure 2-5) [2, 34].

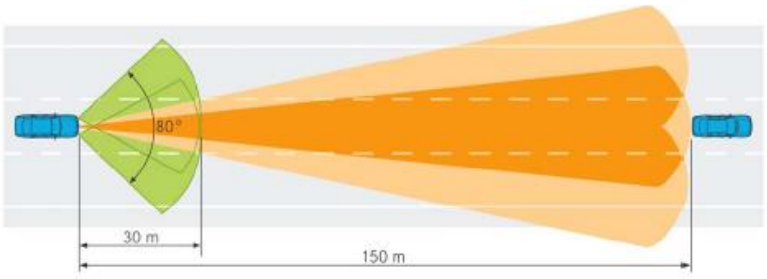

Figure 2-5 Automotive radar range: SRR and LRR

Automotive short-range radar (SRR) can be used for several safety functions in a car, such as parking aid, blind spot detection, crash mitigation and collision avoidance. Figure 2-6 illustrates how SRR is positioned for each application. When potential risk is detected, safety measures can be initiated automatically, such as pre-tensioning of seat belts, inflating airbags, or even automated braking [8].

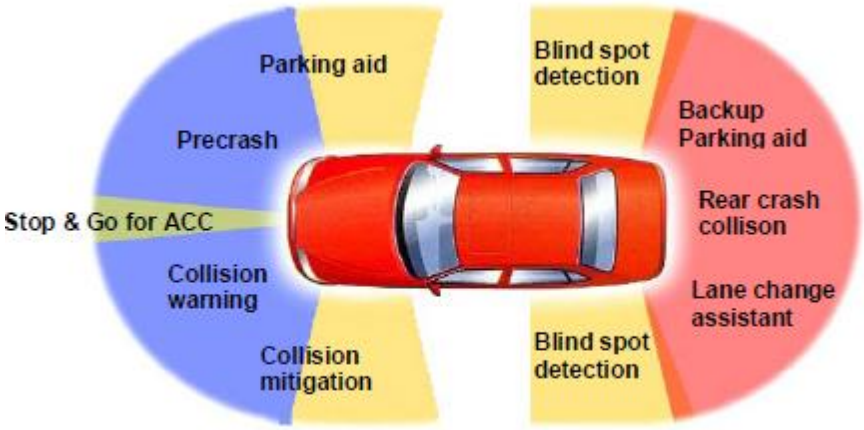

Figure 2-6 Automotive short-range radar

For SRR, lower frequency bands (24 GHz) are preferred over higher frequency bands (79 GHz), since these sensors do not require long-range capability. Moreover, the SRR in the lower bands have the advantages of lower hardware cost and ease of installation. The decrease in cost is mainly due to the analog RF components, since cost tends to increase with frequency and assembly requires more consideration in higher frequency due to the loss.

2.1.3.1.2 Long-range Radar (LRR)

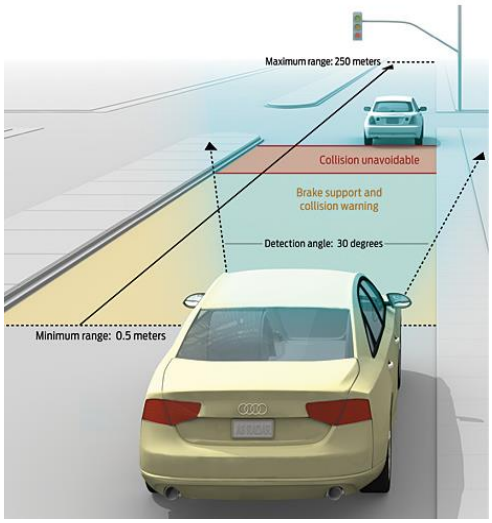

Figure 2-7 Automotive long-range radar

Automotive LRR is usually used to detect potential risk in front of the vehicle. Based on the information provided by the LRR sensor, the ACC can assist the driver with an active breaking system in the event of a sudden hazard appearing in front of the vehicle, or it can smooth the deceleration in other cases.

LRRs measure the range, angle and relative radial velocity of multiple targets with a range of 100 m or higher. However, higher ranges will be at the cost of the accuracy of the target location. For LRR, the upper band is preferred over the lower band for two main reasons: the Doppler discrimination and the angular resolution. The Doppler shift introduced by the relative velocity difference between the source and the target is directly related to the carrier frequency. Thus, the Doppler spread of a 77 GHz radar sensor is three times greater than that of a 24 GHz radar sensor. Moreover, because the beam width of an antenna is proportional to its electrical size, the angular resolution for the same-sized antenna aperture in a 77 GHz radar sensor can be three times that of a 24 GHz one [8, 35].

2.1.3.2 Waveform-based Classification

In this classification, there are two main categories: continuous-wave radars and pulsed radars [30, 38, 39].

2.1.3.2.1 Continuous-wave Radars

Continuous-wave radars use a sinusoidal carrier with or without modulation as a transmit signal. The radar transmits a signal at frequency fT and receives a reflected signal at frequency fS, which is the transmit frequency shifted by the Doppler effect. Koen and Van Caekenberghe demonstrated that the range can be inferred by measuring the frequency of the received signal, and the relationship is given by:

$$R = c\frac{T}{2}\frac{\Delta f}{f_2 - f_1} \quad (1.1)$$

where c is the speed of light, f is the difference between the transmitted and received signal, f_2 and f_1 are the maximum and minimum transmitted frequency, respectively, and T is the period between f_1 and f_2 . The velocity is given by

$$v = \frac{dR}{dt} \quad (1.2)$$

Modulated signals can also be used to measure the range by measuring frequency or phase shift, such as frequency chirp and pseudo-random noise-coding.

2.1.3.2.2 Pulsed Radars

Pulsed radar transmits modulated pulses at periodic intervals of time. Koen and Van Caekenberghe demonstrated that the range can be solved by measuring the time delay between the transmitted pulse and the received echo:

$$R = c\frac{\Delta T}{2} \quad (1.3)$$

where c is the speed of light and T is the time difference between the transmitted and received pulse and echo.

Koen et al. proved that velocity can also be deduced from the Doppler frequency shift between the transmitted pulse and received echo:

$$v = \frac{f_d y_0}{2} \quad (1.4)$$

where f_d is the Doppler frequency shift and y_0 is the free space wavelength at the center frequency.

This type of radar has the disadvantage of the existence of a blind zone where the radar cannot measure the range accurately. This blind range is given by [4]:

$$R_b = c\frac{(\tau_p + t_s)}{2} \quad (1.5)$$

where τ_p is the pulse width and t_s is the switching time of the transmit and receive switch, if applicable. Hence, pulsed radar systems are more suitable for long-range detection and CW radar systems are more suitable for short-range detection. Moreover, in pulsed radar, the transmitter and receiver do not operate simultaneously, which means they operate half-duplex. This results in a high dynamic range and consequently a higher range of detection.

The architecture of pulsed radar is simple to implement, with pulse compression usually performed using the Binary Phase Shift Keying (BPSK) with Barker codes [2, 4, 9].

2.2 Subsystems from Automotive Radar Front-end: BFN

One of the main building blocks of automotive radars is the beam-forming network (BFN). The BFN is a device that feeds the radar antenna array. The purpose of beam-forming is to control the shape of the antenna radiation in order to compress the energy in one direction or the other.

The BFN usually consists of M-input ports and N-output ports, which feed the N array elements, as shown in Figure 2-8. The BFN provides each array element with the required amplitude and phase in order to send the beam in different angles.

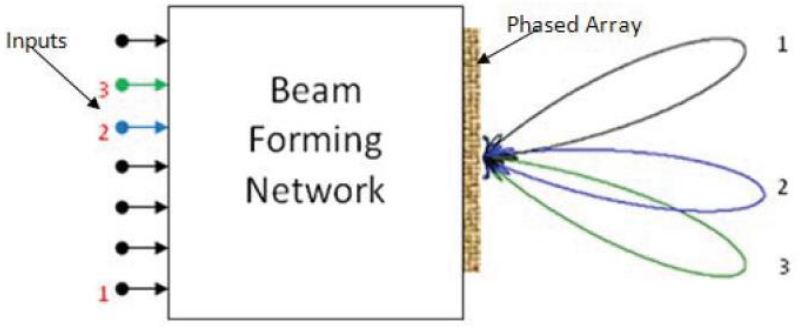

Figure 2-8 Beam-forming network

The three major types of BFNs are digital BFNs, network BFNs, and microwave lens BFNs. These three BFNs will be discussed in detail in the following sections.

2.2.1 Digital Beam-forming Networks

In digital beam-forming networks, the signal-to-feed array elements are created digitally using a general purpose processor or a dedicated processor, such as a digital signal processor (DSP). These elements are then converted to analog using a digital-to-analog converter (DAC).

The advantage of this technique is the accuracy of the signal generated and the fine-tuning that can be performed. However, it has the drawback of a limited output frequency range due to the computation speed of the processor and the sampling rate of the DAC.

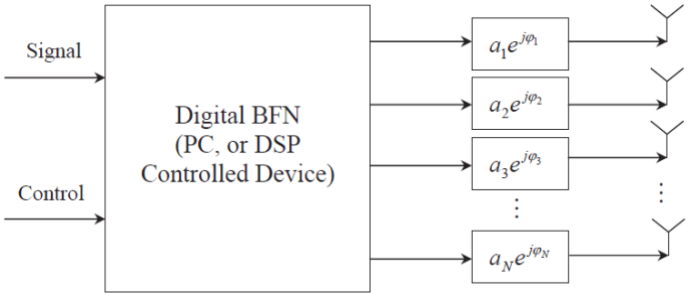

Figure 2-9 Digital beam-forming network

2.2.2 Matrix Beam-forming Networks

Three main techniques fall into this category of BFN, namely the Butler matrix, the Blass matrix, and the Nolen matrix. The Butler matrix is one of the earliest BFNs and consists of alternate rows of hybrid junctions and fixed phase shifters, as shown in Figure 2-10.The Blass matrix is simple to implement but is less than ideal in its functioning, as the beam shift is dependent on the transmitted frequency. The Blass matrix BFN makes use of directional couplers to connect the beam port line to the array element transmission lines, and the Nolen matrix BFN can be considered a combination of the Blass and Butler matrices.

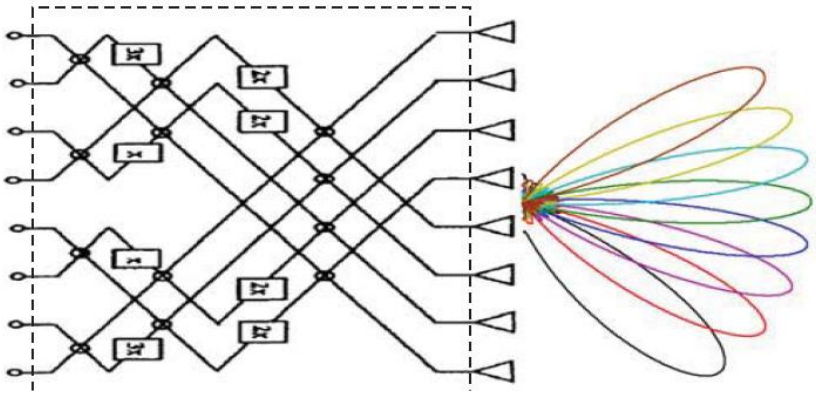

Figure 2-10 Matrix beam-forming network

2.2.3 Microwave Lens Beam-forming Networks

Microwave lens BFN is a technique based on the path delay mechanism to modify the phase of the signal at the input of each array element. A typical microwave lens BFN diagram is shown in Figure 2-11.

The lens geometries vary with cavity type, such that if the cavity is homogeneous, the lens geometries follow the focal lens design approaches such as Rotman lens, whereas if the cavity is inhomogeneous, the lens geometries follow the ray path equation as the function of refraction index, such as Luneberg's lens.

Homogeneous lenses can be implemented using several different materials, and each approach has its benefits. So, for instance, it can be implemented in waveguide to achieve high output power, in striplines to achieve wide bandwidth, and in microstrip to achieve low profile [48].

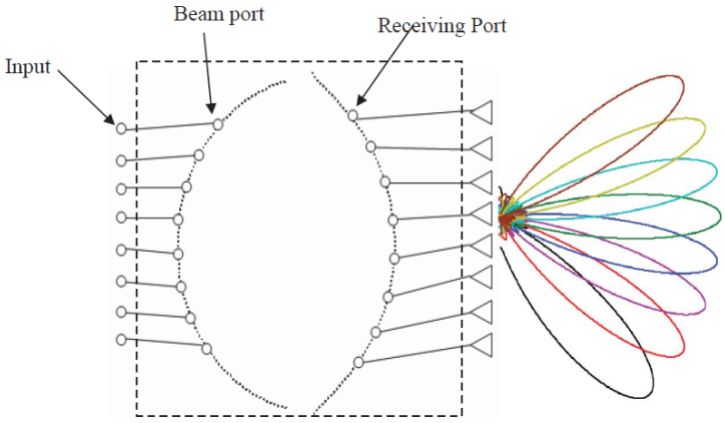

Figure 2-11 Microwave lens beam-forming network

2.3 Automotive Radar Front-end RF-MEMS Components

Among RF MEMS circuits and devices in the context of 77GHz radar, we can find RF MEMS switches, tunable capacitors, phase shifters, reconfigurable antennas and matching circuits, all of which are good candidates for automotive radar applications. This section first presents a focused literature review of RF-MEMS switch components and then provides a brief introduction to the others.

2.3.1 RF MEMS Switches for Millimetre Wave Applications

Compared to other semiconductor components, RF MEMS switches have several advantages: low insertion loss, high signal linearity, high isolation, very low power consumption and wide bandwidth. Like micro-components, RF MEMS switches are mass-fabricated on semiconductor wafers, which results in high product uniformity, low cost, and ease of integration with other semiconductor components. However, RF MEMS switches still suffer from reliability issues, low switching, low power handling and integration processes in non-standardized process flows (Oberhammer, 2004). In the literature, two main classes of RF MEMS switches can be found; metal-contact series switches and capacitive shunt switches. A schematic of these two types of switches is shown in Figure 2-12.

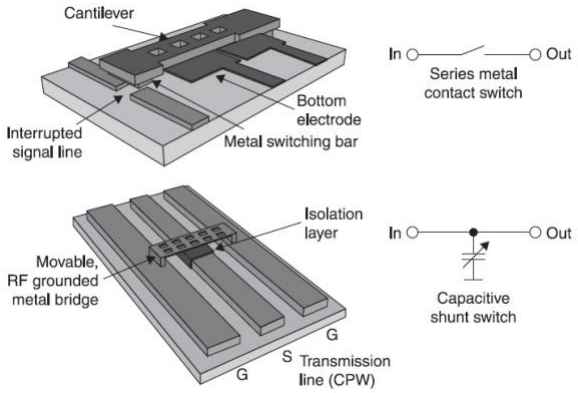

Figure 2-12 Metal-contact series switches and capacitive shunt switches

The series switch family with metal contacts consists of a cantilever and a metal that connects the main signal line, resulting in a direct ohmic contact. Theoretically, this switch is capable of handling RF signals up to 100 GHz; however, at high frequency, it has low isolation due mainly to the up-state capacitance and substrate wave coupling.

The second family of switches, capacitive shunt switches, consist of a metal bridge connected to the RF ground and switching above the signal line. An isolation layer is added between the bridge and

signal line. The concept of this switch is that the bridge is used to short-circuit the signal line to the ground through a capacitance which makes its off-state. Some of the drawbacks of this switch include the handling of the parasitic inductance, which limits its performance [2, 5, 20].

Table 2-1 Examples of Typical RF MEMES Switches

Device	Actatuation Voltage (V)	Insertion Loss (dB) at 77GHz	Isolation (dB) at 77 GHz
Capacitive series switch	N/D	0.3	17
T-match capacitive shunt switch	30	0.25	20
π -match capacitive shunt switch	30	0.4	30
Longitudinal coplanar shunt switch	25	0.3	30
T-match and π -match capacitive shunt switch on quartz substrate	40	0.2-0.5	25
Metal- to-metal contact shunt switch	22	1	22
DC contact series switch	39	0.36	17.3

2.3.2 RF MEMS Tunable Capacitors

Tunable capacitors have many applications, especially in automotive radars. The tuning is achieved through varying the gap between the parallel plates of the capacitance or by changing the overlapping area between a fixed and a moving electrode. The schematic of the RF MEMS capacitor with a tunable gap between parallel plates is similar to the RF MEMS capacitive shunt switches, but with the addition of more tuning states between the down- and up-states. These types of capacitors are characterized by a high Q factor but suffer from limited tuning range and the non-linearity effects of analog tuning [2, 9].

2.3.3 RF MEMS Phase Shifters for Millimeter Waves Applications

RF MEMS phase shifters are used in phased antenna arrays, which are a part of the radar system. These types of shifters are characterized by their linear behavior, good power efficiency, and low insertion loss over their solid-state homologue. Additionally, RF MEMS phase shifters are easy to integrate and relatively cheap compared to ferrite-based phase shifters.

The three main types of MEMS phase shifters mentioned in the literature are MEMS-switched true-time delay-line (TDD) phase shifter networks, distributed MEMS transmission line (DMTL) phase shifters, and MEMS tunable dielectric-block loaded-line phase-shifters [43, 46].

2.4 Waveguide-Switch Technologies

A mechanical switch is one that achieves switching by mechanically connecting or breaking a signal path. It can be controlled either electronically or mechanically. A typical RF mechanical switch is controlled by an electrical signal. In most cases, electromagnetic relays are used. Considering the same technology as mechanical switches, typical waveguide switches change position by rotation. In general, switching at high frequencies can be done either by using a rotary electrical motor (to make or break the waveguide path) or by incorporating a PIN diode inside the waveguide acting as a switch (Figure 2-13). A third method is to incorporate RF microelectromechanical (MEMS) switching devices in the waveguide. This method benefits from the general advantages of RF MEMS switches, such as good RF performance and small size.

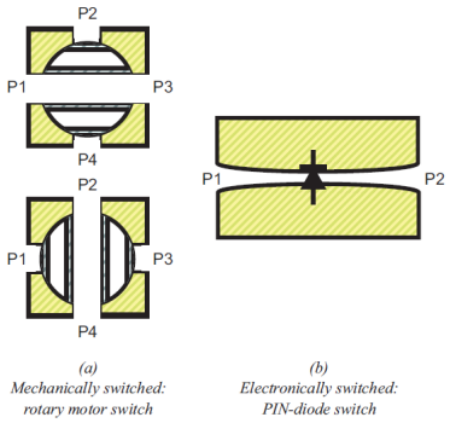

Figure 2-13 Typical waveguide switches [5]

To the best of our knowledge, the waveguide switch presented by M. Daneshmand et al. [5] is the only publication that uses MEMS for waveguide switching. In the work, MEMS thermally plastic

deformable actuators have been integrated with a ridge waveguide to construct the switch (Figure 2-14), while a combination of vertical contact cantilevers is used to switch the wave propagation in the waveguide ON or OFF. For this waveguide switch, a return loss of better than 15 dB, an insertion loss of 1-2.8 dB, and an isolation of better than 15 dB was achieved [19].

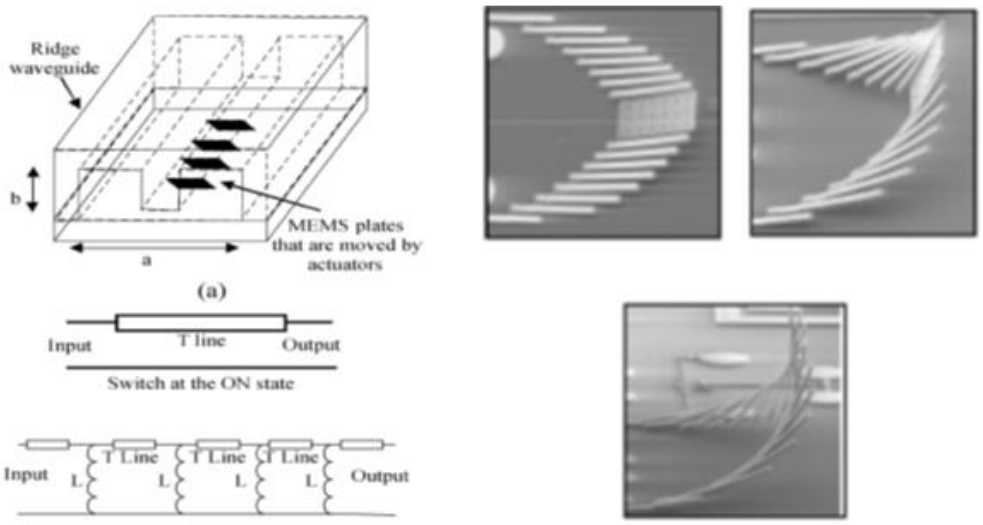

Figure 2-14 MEMS-waveguide switch developed at CIRFE [5]

2.5 Waveguide-to-CPW Transitions

Radar antennas have been designed and implemented based on micromachined waveguides, but active MMIC modules are implemented on planar transmission lines. Hence, a reliable transition from on-wafer waveguides to planar transmission lines is essential to realize fully integrated systems.

A number of transition approaches, ranging from planar transmission lines to rectangular waveguide using microfabrication technology for W-band and higher frequencies, have been reported in the literature [6]. All of these transitions have complex 3D geometries that require the assembly of various parts. Considering the dimensions in mmw and terahertz regions, implementing the transitions with acceptable accuracy becomes very difficult. So, fully micromachined transitions which do not require assembly of parts are preferred for these high frequency applications. A 2.5D fully micromachined resonant-based transition is proposed in [50]. In this design, the transition is realized using two resonant structures: a shorted section of transmission line with a pin inside the waveguide, and an E-plane step discontinuity.

Here, the configuration and design procedure for developing a full-band transition from a CPW line to a rectangular waveguide is presented. It should be emphasized that the transition topology is chosen in such way that it can be easily fabricated using silicon micromachining. To achieve a broadband response, the transition is realized in three steps. The first step is a tapered transition from a CPW line to a reduced-height waveguide with the same impedance. The second and third steps are novel in-plane wedge impedance tapers from the reduced-height waveguide to the final waveguide height (Figure 2-15).

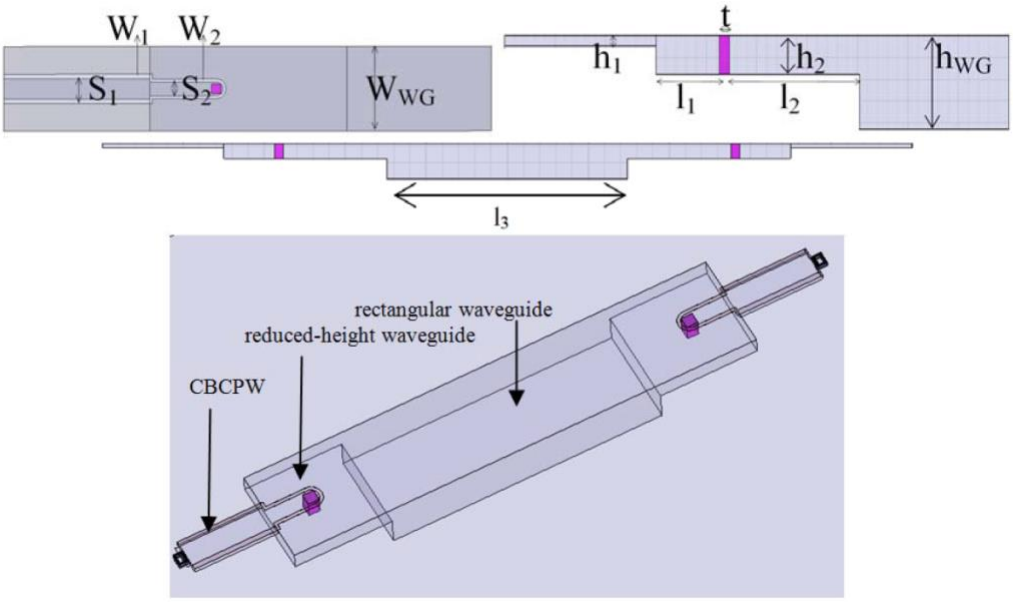

Figure 2-15 CPW-to-waveguide transition [6]

The microfabrication process includes the usage of two wafers: a bottom wafer and a top one. The fabrication of the bottom wafer involves three major steps (Figure 2-16). In the first step, the multi-step components are etched on the top side of the wafer using a deep reactive ion etching (DRIE) process. The second step involves etching through the wafer from the backside to create openings for chip integration. In the final step, the surface of the wafer is coated with a layer of gold (Figure 2-17) [42, 49].

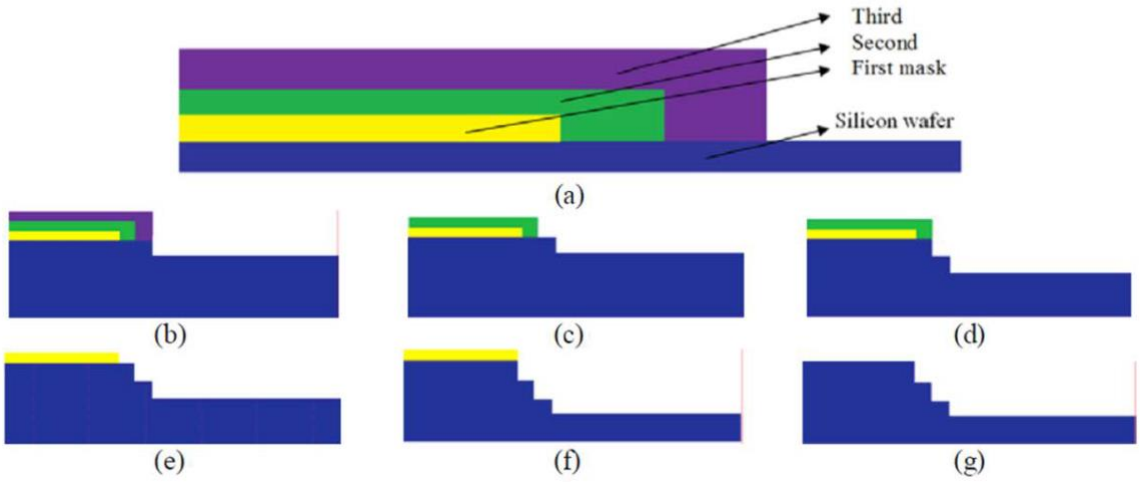

Figure 2-16 DRIE steps for bottom wafer [6]

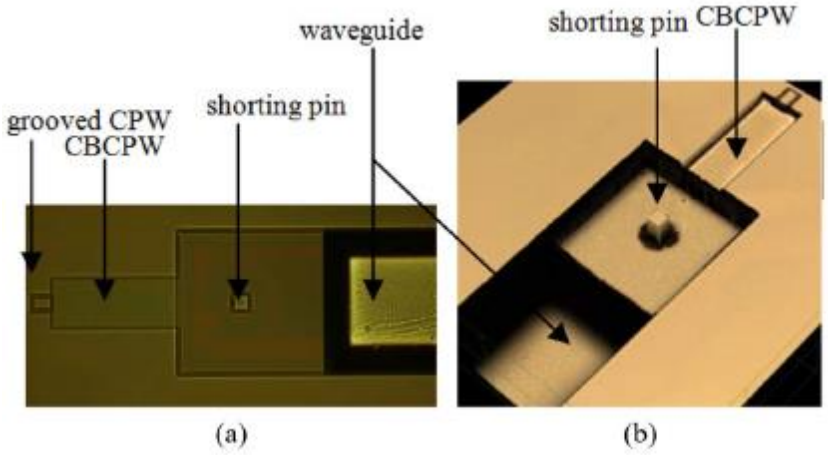

Figure 2-17 Bottom wafer after etching and metallization [6]

The top wafer (Figure 2-18) is used to cover the top part of the waveguide structure. On this wafer, a stacked layer of LPCVD SiO2/Si3N4/SiO2 membrane is first deposited. This three-layer membrane is chosen to minimize stress so that the membrane does not buckle after the top silicon is removed [27].

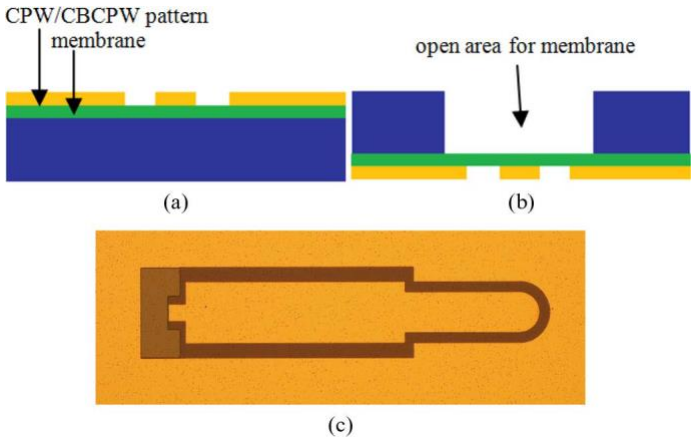

Figure 2-18 Top wafer [6]

2.6 Automotive Radar Front-end Developed in Academia

2.6.1 University of Windsor Front-end

Several research projects were carried out on automotive radar at the University of Windsor. This research was validated on an automotive radar system test bed located at the university.

2.6.1.1 Radar System Overview

This automotive radar system is intended to work in the 76 - 77GHz frequency band and on three different modes: Long-range radar (LRR), medium-range radar (MRR), and short-range radar (SRR). The block diagram of that system is shown in Figure 2-19 [24].

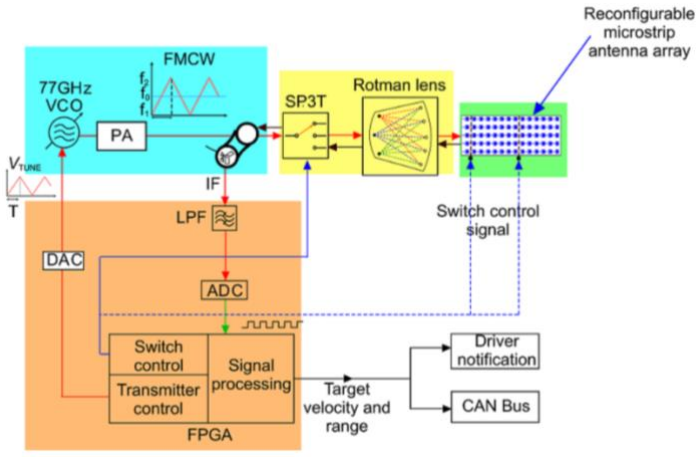

Figure 2-19 Block diagram of Windsor automotive radar system [24]

The major components of the MEMS based tri-mode radar are [7]:

- Microfabricated Rotman lens
- MEMS SP3T RF switches
- TLC MINT77TR GaAs transceiver
- MEMS reconfigurable microstrip antenna array
- MEMS SPST RF switches
- FPGA/ASIC implemented controller

2.6.1.2 Principle of Operation

2.6.1.2.1 Transmitting side:

A transmitter circuit, comprising an FPGA, digital-to-analog converter (DAC) and voltage-controlled oscillator (VCO), generates a linear frequency-modulated continuous wave (LFMCW) signal that feeds the MEMS SP3T switch. The control signal is triggered by the FPGA in order to switch between the steering directions. The signal then travels through the Rotman lens to reach the microstrip antenna and is radiated in a specific direction. The microstrip antenna array is adjusted by MEMS SPST switches which, in turn, are controlled by the FPGA [32].

2.6.1.2.2 Receiving side:

The radiated signal is received by the microstrip antenna array and is reflected off a vehicle or an obstacle. The signal is then transported by the microstrip antenna array and fed to the SP3T switch through the Rotman lens. Next, the signal is down-converted into an IF signal in the range of 0-200 KHz and digitized by the analog-to-digital converter (ADC). Finally, the received digital signal is processed inside the FPGA to determine the position of the detected signal [7, 11].

2.6.2 University of Michigan RF MEMS Radar Front-end

Van Chekenberghe and Sarabandi, at the University of Michigan, developed a 38-GHz high-pulse repetition frequency (HPRF) mono-pulse Doppler-radar front-end for long-range automotive radar applications [26].

2.6.2.1 Radar System Overview

The main building blocks of this radar system are the RF MEMS electronically scanned array (ESA) and low-loss MEMS time-delay units (TDU). The system's characteristics are as follows:

- Range: 150m
- Resolution: 1.5m
- Scanning angle resolution: ±11° in the Azimuth plane, with an angular deviation of ±2.5°

A diagram of the radar system is shown in Figure 2-20.

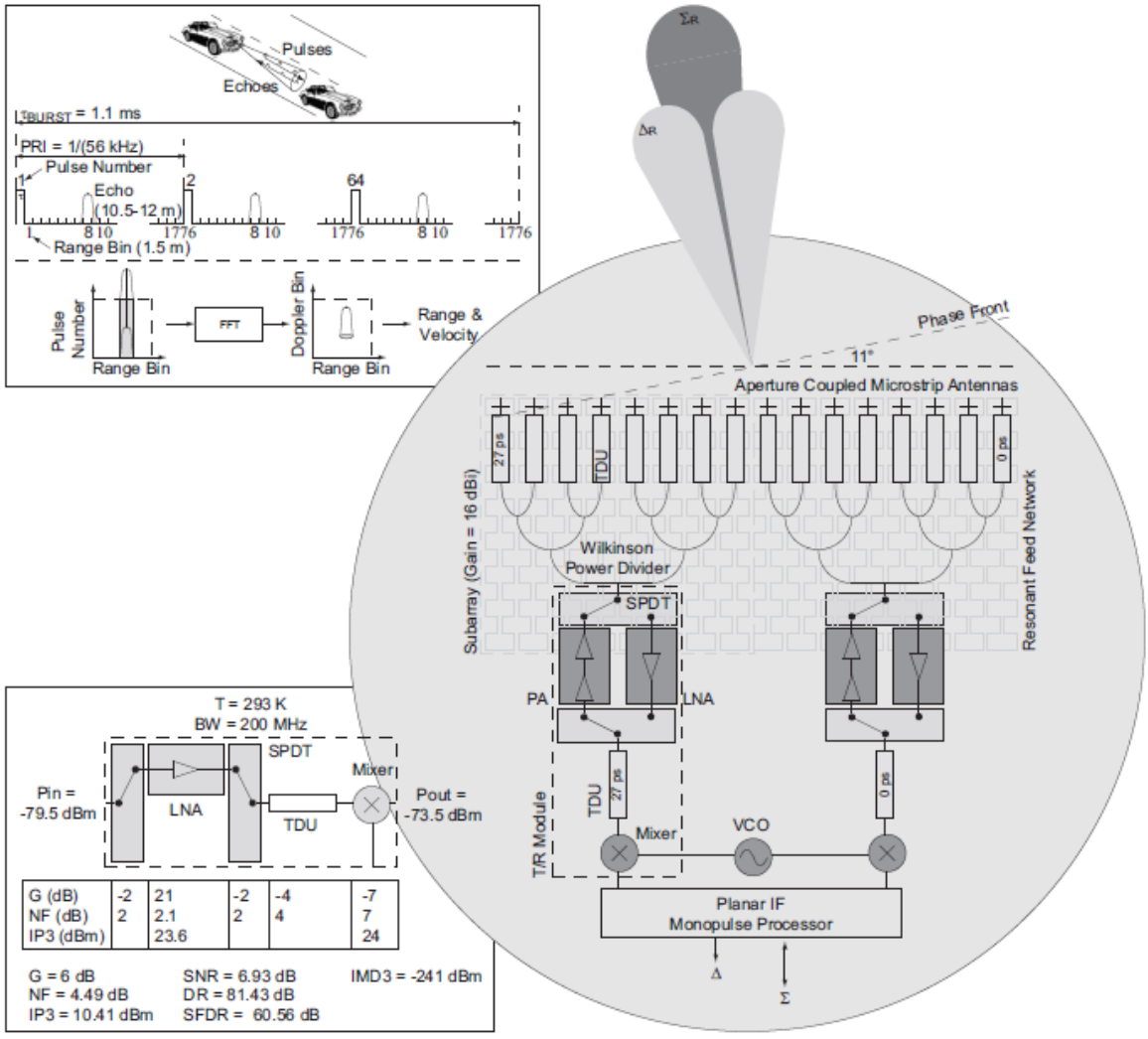

Figure 2-20 University of Michigan radar system

As shown in Figure 2-20, the radar front-end comprises a transceiver module, an IF impulse processor, and two passive sub-arrays [2, 41].

2.6.2.2 Principle of Operation

2.6.2.2.1 Transmitting side:

The IF impulse processor feeds the transmitter module with the signal, which in turn feeds a Wilkinson divider. After the signal is split, it is fed to the line antenna arrays to be radiated.

2.6.2.2.2 Receiving side:

The received signal is divided into the sum (Σ) and azimuth (A) for processing and is then used to correct the angular error.

2.6.3 Braunschweig University of Technology and Robert Borsch

Schoebel et al. developed two designs for automotive radar front-end. The first design uses Wilkinson power dividers to feed RF MEMS phase shifters, and the second design uses a MEMS single-pole multi-throw switch to select one of several beams of a planar Rotman lens. These two designs work at 77 GHz and are shown in Figure 2-21 [9].

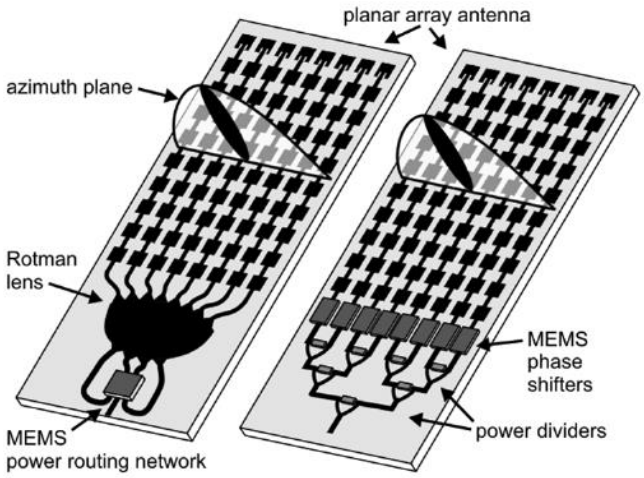

Figure 2-21 First and second designs of the automotive radar front-end

2.6.3.1 Theory of Operation

In the first design, three stages of 2-port Wilikinson power dividers in association with RF MEMS stub-loaded line phase shifters construct the desired beam to feed the patch antenna array. This automotive radar design is based on MEMS capacitive shunt switches, offering a 90 and 180° phase shift and a less than 4° phase tolerance. Figure 2-22 shows a photo of the design [2].

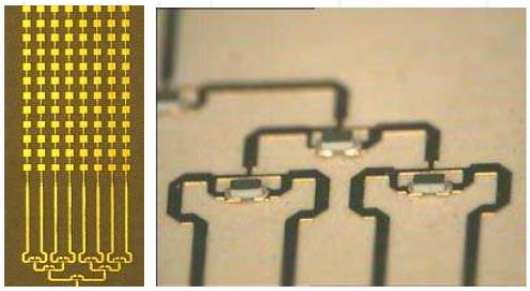

Figure 2-22 Wilkinson power dividers

For the second design, a single-pole quadruple-throw (SP4T) switch selects the input of the Rotman lens to form the desired beam to feed the patch antenna array. Figure 2-23 illustrates the fabricated MEMS automotive radar based on the Rotman lens and SP4T switch [9, 11, 40, 44, 45].

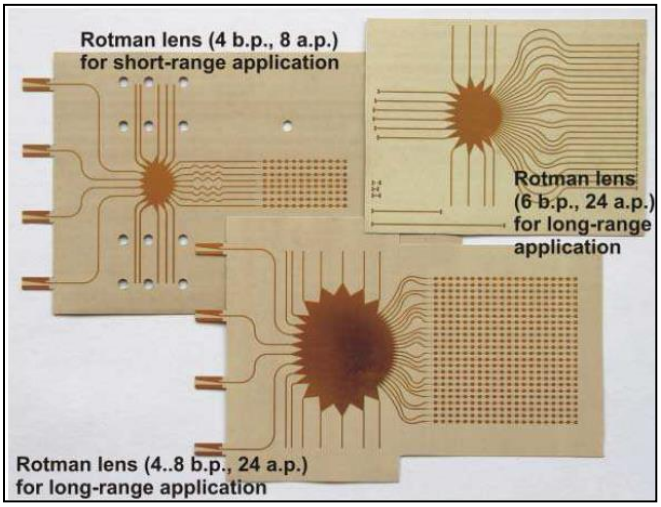

Figure 2-23 Rotman lens for the second design

The radiation patterns of the two designs with the same microstrip antenna array are shown in Figure 2-24 below.

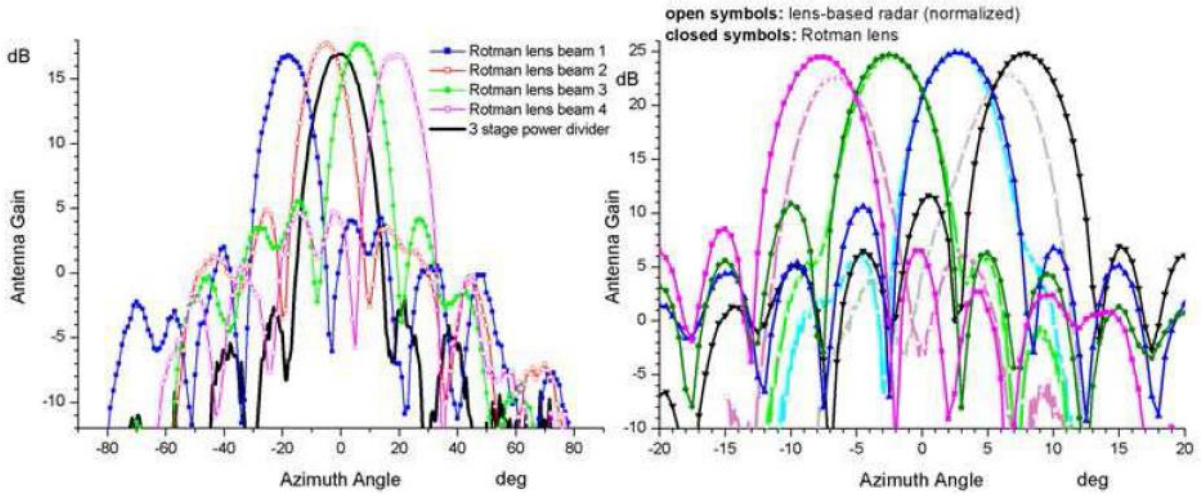

Figure 2-24 a) Antenna patterns for Wilkinson divider and first Rotman lens; b) antenna pattern for 8-beam port Rotman lens [13]

2.6.4 NORDITE-SARFA RF MEMS for Automotive Radar (77 GHz)

SARFA is a project in the NORDITE Scandinavian ICT program. It focuses on RF MEMS for improving the performance and decreasing the cost of beam-steering units that are utilized in 77 GHz automotive radar sensors. SARFA collaborates with NTNU Trondheim, Norway, and TKK Espoo/Helsinki, Finland, and is supported by ten Scandinavian industrial partners in automotive electronics, MEMS fabrication, and telecommunications [2].

This project of designing the automotive radar front-end is divided into two phases. The first phase involves the design of MEMS tunable high-impedance surfaces for beam-steering and reconfigurable phase shifters, and the second phase consists of the integration of transmission-line-based MEMS phase shifters based on electromechanically tunable dielectrics with antenna elements.

2.6.4.1 Theory of Operation

After being radiated by the patch-antenna array, the beam is steered through the phase shift, which is realized by the MEMS tunable high-impedance surface. These MEMS tunable high-impedance surfaces can be placed on sidewall inclusions of a rectangular metal waveguide and can allocate a differential analog phase shift from 0 to 240°. Figure 2-25 shows this automotive radar front-end design [28].

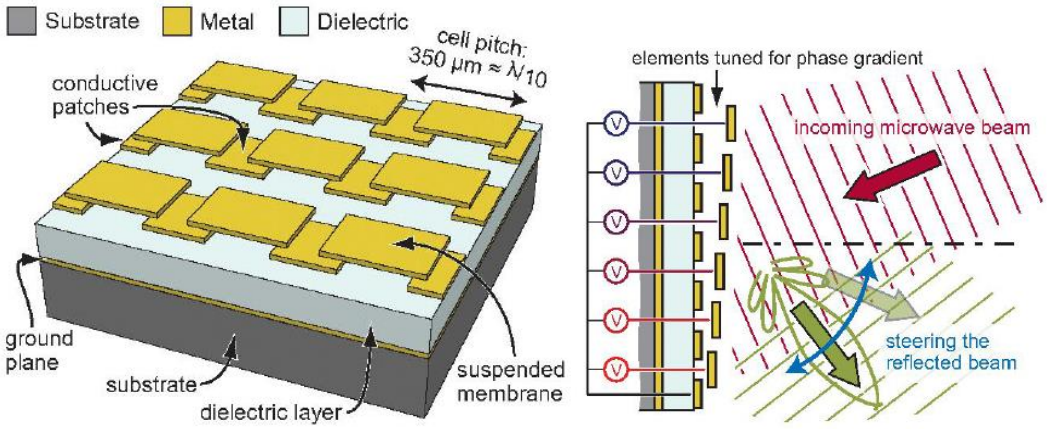

Figure 2-25 Automotive radar front-end

2.7 Automotive Radar Front-end Developed in the Industry

2.7.1 Classic Automotive Radar Sensors

Table 2-2 Classic Automotive Radar Sensors

Radar Supplier	Waveform	Range (m)	FOV (°)	Scanning
Fujitsu Ten	FM-CW	120	16	Mechanical 8 beams
Mitsubishi	FM-Pulse	150	12-16	Mechanical 8 beams
Denso	N/D	150	20	N/D
NEC	FM-CW	120	16	Synchronized 9 beams
Hitachi	FSK	120	16	Monopulse
A.D.C	FM-CW	150	10	Switched 3 beams
Bosch	FM-CW	150	8	Switched 3 beams
Delphi	FM-CW	150	12	Mechanical
Eaton	FSK	150	12	Monopulse
Visteon	FSK	150	12	Monopulse

2.7.2 New Trends in Radar Front-end Systems

2.7.2.1 Freescale

The semiconductor leader Freescale proposes automotive radar architecture based on its own chipset. As Figure 2-26 shows, this type of radar consists of the baseband chip Qorivva MPC577xK MCU, a VCO (MRD2001VC), a two-channel Tx transmitter (MRD2001TX), and a three-channel Rx receiver (MRD2001RX) [56].

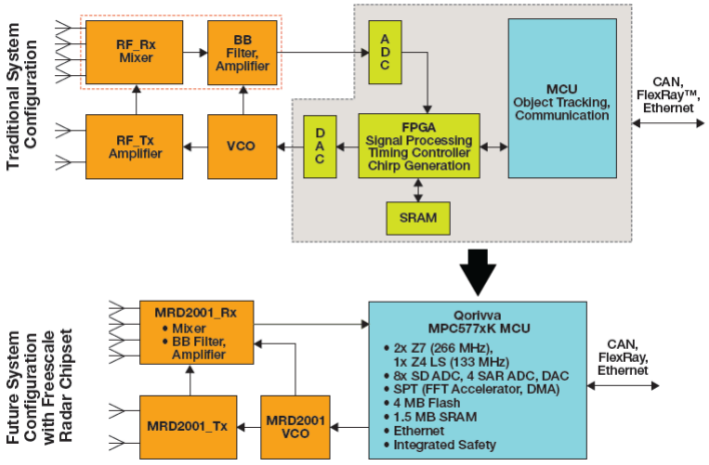

Figure 2-26 Freescale automotive radar front-end

The Qorivva MPC577xK MCU chip includes all the necessary components for signal processing, data conversion and memory, since it comprises an FPGA, ADC, DAC and SRAM. The inclusion of these components reduces the overall number of components required, as well as PCB size and software complexity. A block diagram of this chip is given in Figure 2-27

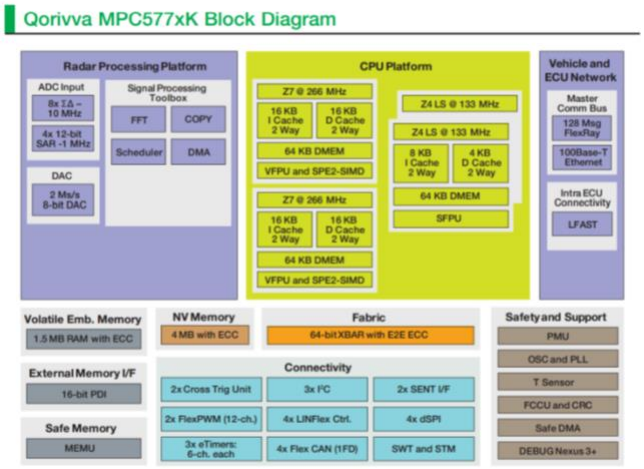

Figure 2-27 Qorivva MPC577xK block diagram

2.7.2.2 Infineon

Figure 2-28 shows the Infineon solution for a 76-77 GHz radar complete proximity system. Infineon has been producing their RASIC™ technology chips since 2009. The 77GHz SiGe MMIC segment can be used in various configurations to build RF front-end modules for sensors in applications such as LRR, as well as in collision mitigation (CM) and emergency brake assist (EBA) features. Essentially, the technology has a 4-channel transceiver for use in 2Tx-4Rx systems (different antenna configurations can be supported), a dielectric reference oscillator/mixer (DRO) RON7701 for PLL-based systems, a programmable modulation waveform generation and PLL frequency control, and the new family of microcontroller AURIX™ that has a multicore architecture based on three independent 32-bit CPU [57].

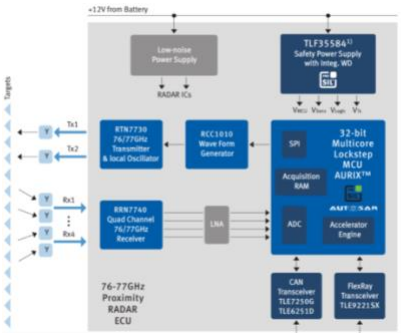

Figure 2-28 Infenion automotive radar

2.7.2.3 Triquint

Triquint developed solutions for the long- and medium-range automotive radar market with a wide portfolio of 77 GHz MMICs for front-end applications. Figure 2-29 presents a block diagram of a proposed 77 GHz radar. It is basically a multi-die discrete structure composed of a 19 GHz oscillator, 19 GHz to 77 Ghz doublers, a 77 GHz SP3T Tx, a 77 Ghz SP4T Rx, a 77 GHz LNA, and a mixer [23].

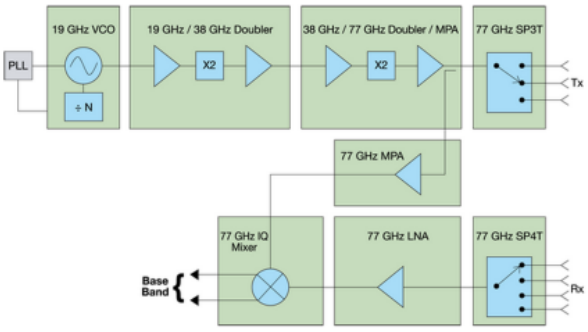

Figure 2-29 Triquint automotive radar

2.7.2.4 NXP

NXP has a portfolio of LDMOS transistors supported by a strong portfolio of SiGe:C-based discretes and ICs for L and S band radar systems that are well-suited for analog, digital and hybrid beam-forming implementations (Figure 2-30) [58].

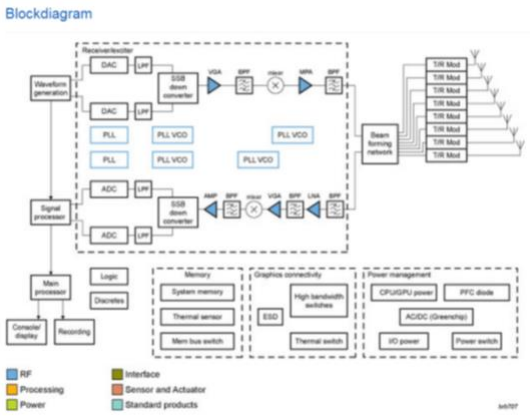

Figure 2-30 NXP automotive radar

Chapter 3
Rotman Lens and 2D Beam-forming Network

This chapter presents a set of simulations along with theoretical and experimental work related to Rotman lens design. It also briefly addresses some major design considerations in RF-MEMS switches for beam-forming networks.

3.1 Microwave Rotman Lens

In Chapter 2, the Rotman lens was presented as an example of a beam-forming network. In this section, we present a detailed approach to generating a Rotman lens based on certain specifications. Microwave lenses appeared during the 1950s as a beam-forming network (BFN) to respond to specific limitations in several applications. The Rotman lens was then developed to enable the functioning of a true-time delay (TTD), compact, multi-beam, wideband and passive device. Along with the development of materials science and fabrication technologies, new implementations of the Rotman lens in stripline, microstrip and substrate integrated waveguide (SIW) have been proposed. The key features of the Rotman microwave lens are presented in Figure 3-1.

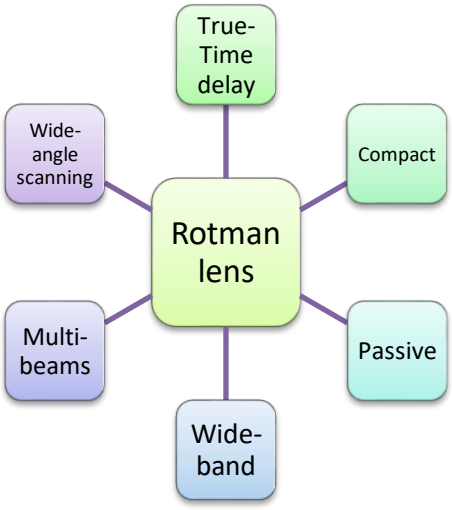

Figure 3-1 Rotman lens specifications

3.1.1 Rotman Lens Design

Figure 3-2 outlines the steps adopted in the design and development of a Rotman lens. The five major steps are: Rotman lens specifications, geometry derivation, transmission line implementation, performance simulations, and fabrication and measurement.

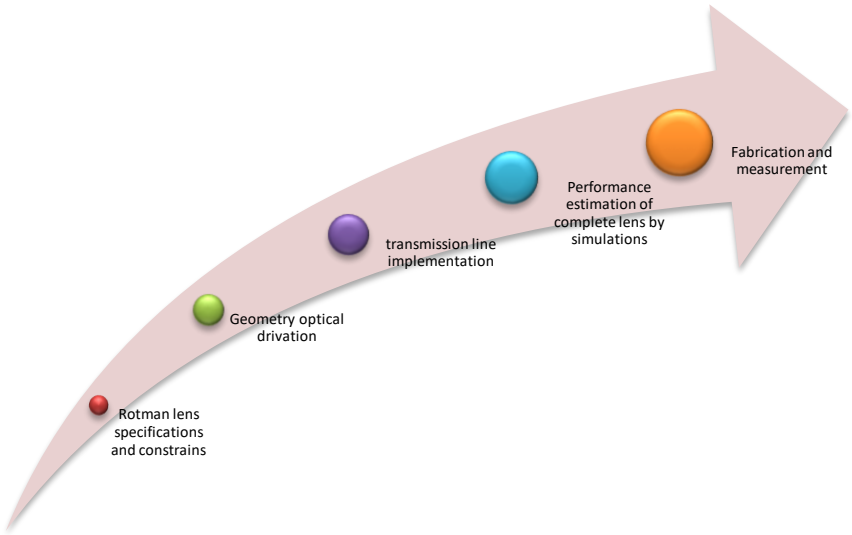

Figure 3-2 Rotman lens design method

We categorize the target specifications of the Rotman lens into two groups: electrical and mechanical. Electrical specifications consist of phase errors, amplitude errors, maximum scanning angle, return loss, bandwidth, power efficiency and maximum power sustained. The mechanical specifications include size, weight, etching/milling tolerance, temperature range, robustness, resilience and sustainability (Table 3.1). A trade-off in the design is imposed, as some requirements cannot be met in the same design. However, reasonable design specifications can usually be fulfilled in one or more of the designing steps [10, 11].

Table 3-1 Microwave Lens Specifications

Microwave Lens **Electrical Specifications**	**Microwave Lens** **Mechanical Specifications**
Phase errors	Size
Amplitude errors	Weight
Maximum scanning angle	Etching/milling tolerance
Return loss, Bandwidth	Temperature range
Power efficiency	Robustness
Maximum sustainable power	Cost of fabrication

3.1.2 Rotman Lens Design Geometry Derivation and MATLAB Simulation

3.1.2.1 Rotman Lens Optical Geometry Derivation

In Figure 3-3, the lens contours are shown by the curves $\sum_1$ and $\sum_2$. The inner contour $\sum_1$ is determined by the lens equations and locates the position of the probe transitions between the lens and the microstrip line to arrays. The outer contour $\sum_2$ is straight and defines the position of the radiating elements that compromise the line source.

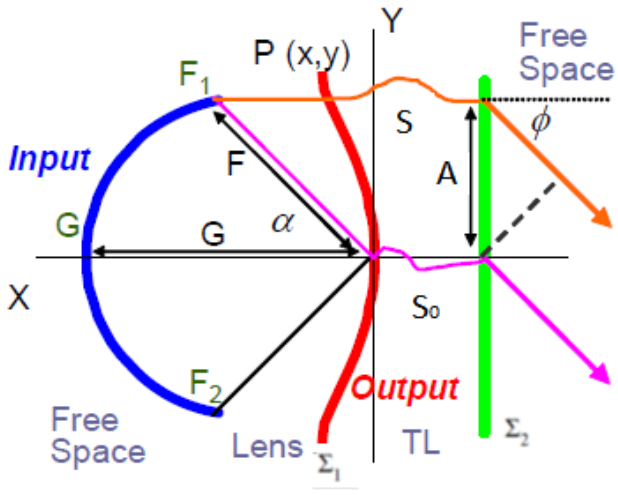

Figure 3-3 Rotman lens geometry presentation

Corresponding elements on contours $\sum_1$and $\sum_2$ are connected by microstrip lines. The scan angle ϕ is the same as a focal angle in the design.

The contour $\sum_1$is is defined by the two coordinates (X,Y) that are specified relative to point O on the center axis of the lens. Elements on the straight contour $\sum_2$ are similarly determined by the single coordinate A, measured relative to the point O. This point (O) lies on the contours $\sum_1$ and $\sum_2$, and is connected by a transmission line of electrical length S. The point $P(X,Y)$ is connected to a typical element $Q(A)$, which lies on $\sum_2$ by the transmission line of electrical length S. Since the three parameters X, Y and S are independent, the straight-front-face lens has three degrees of freedom to be stipulated. These three degrees of freedom are used to obtain wide-angle scanning characteristics by selecting two symmetrical off-axis focal points F_1 and F_2 and one on-axis focal point G, with coordinates $-(F\cos\alpha, F\sin\alpha)$, and $(-G_1, 0)$, respectively, relative to point O. A central ray which passes through the origin of the lens is represented by $\overrightarrow{F_1P}$, with $\overrightarrow{F_1PQK}$ representing any other ray which originates from point F_1, while F_1, F_2 and $G_1$are points of perfect focus for radiation at angles to the axis of $-\alpha, +\alpha$ and 0^0, respectively. The electrical wavelength λ_g in the lens is approximated to $\frac{\lambda_0}{\sqrt{\varepsilon_r}}$, and $\lambda_g$in the microstrip line is $\frac{\lambda_0}{\sqrt{\varepsilon_{eff}}}$. So, these electrical wavelengths should be considered in the derivations of the lens equations. The equations for optical path-length quality between a general ray and the ray through the origin become:

$$\overrightarrow{F_1P} + \frac{\sqrt{\varepsilon_{eff}}}{\sqrt{\varepsilon_r}}S + \frac{1}{\sqrt{\varepsilon_r}}A\sin\alpha = F + \frac{\sqrt{\varepsilon_{eff}}}{\sqrt{\varepsilon_r}}\,S_0, \qquad (3.1)$$

$$\overrightarrow{F_2P} + \frac{\sqrt{\varepsilon_{eff}}}{\sqrt{\varepsilon_r}}S - \frac{1}{\sqrt{\varepsilon_r}}A\sin\alpha = F + \frac{\sqrt{\varepsilon_{eff}}}{\sqrt{\varepsilon_r}}\,S_0, \qquad (3.2)$$

and

$$\overrightarrow{(G_1P)} + \frac{\sqrt{\varepsilon_{eff}}}{\sqrt{\varepsilon_r}}S = G + \frac{\sqrt{\varepsilon_{eff}}}{\sqrt{\varepsilon_r}}S_0 \qquad (3.3)$$

where

$$\overrightarrow{(F_1P)^2} = F^2 + X^2 + Y^2 + 2FX\cos\alpha - 2FX\sin\alpha \qquad (3.4)$$

$$\overrightarrow{(F_2P)^2} = F^2 + X^2 + Y^2 + 2FX\cos\alpha + 2FX\sin\alpha \qquad (3.5)$$

and

$$\overrightarrow{(GP)^2} = (G + X)^2 + Y^2 \qquad (3.6)$$

$\overrightarrow{F_1P}, \overrightarrow{F_2P}$ and $\overrightarrow{GP}$ are the path lengths from focal points F_1, F_2 and G_1, respectively, to point P on the inner lens contour. A set of parameters which are normalized relative to the focal length F is now defined as:

$$x = \frac{X}{F}, y = \frac{Y}{F}, g = \frac{G}{F}, \eta = \frac{A}{F}, s = \frac{S}{F}, a_0 = \cos\alpha, b_0 = \sin\alpha$$

So, Equations (3.4) to (3.6) now become

$$\frac{\overrightarrow{(F_1P)^2}}{F^2} = 1 + x^2 + y^2 + 2a_0x - 2b_0y,$$

$$\frac{\overrightarrow{(F_2P)^2}}{F^2} = 1 + x^2 + y^2 + 2a_0x - 2b_0y$$

and

$$\frac{\overrightarrow{(GP)^2}}{F^2} = (g + x)^2 + y^2$$

and the normalized forms of (3.1) and (3.4) are combined as:

$$\frac{\overrightarrow{(F_1P)^2}}{F^2} = \left(1 - \frac{\sqrt{\varepsilon_{eff}}}{\sqrt{\varepsilon_r}}S - \frac{1}{\sqrt{\varepsilon_r}}b_0\eta\right)^2$$

$$= 1 + \frac{\varepsilon_{eff}}{\varepsilon_r}S^2 + \frac{1}{\varepsilon_r}{b_0}^2\eta^2 - \frac{1}{\sqrt{\varepsilon_r}}2b_0\eta + \frac{\sqrt{\varepsilon_{eff}}}{\varepsilon_r}2b_0S\eta - \frac{\sqrt{\varepsilon_{eff}}}{\sqrt{\varepsilon_r}}2S$$

$$= 1 + x^2 + y^2 + 2a_0x - 2b_0y \qquad (3.7)$$

Since the off-axis focal points are located symmetrically around the center axis, the lens contours must also be symmetrical. Therefore, Eq. (3.7) remains unchanged and can be separated into two independent equations if η is replaced by $(-\eta)$ and y by $(-y)$. One equation contains only odd powers of y and η, while the other contains the even terms. Thus,

$$-\frac{1}{\sqrt{\varepsilon_r}}2b_0\eta + \frac{\sqrt{\varepsilon_{eff}}}{\varepsilon_r}2b_0S\eta = -2b_0y, \qquad (3.8)$$

or

$$y = \frac{1}{\varepsilon_r}\eta\left(1 - \frac{\sqrt{\varepsilon_{eff}}}{\sqrt{\varepsilon_r}}s\right)$$

and also

$$x^2 + y^2 + 2a_0x = \frac{\varepsilon_{eff}}{\varepsilon_r}s^2 + \frac{1}{\varepsilon_r}{b_0}^2\eta^2 - \frac{\sqrt{\varepsilon_{eff}}}{\sqrt{\varepsilon_r}}2s \qquad (3.9)$$

Equations (3.3) and (3.6), relating to the on-axis focus, are likewise combined:

$$\frac{\overrightarrow{(GP)^2}}{F^2} = \left(g - \frac{\sqrt{\varepsilon_{eff}}}{\sqrt{\varepsilon_r}}S\right)^2 = (g+x)^2 + y^2, \qquad (3.10)$$

or

$$x^2 + y^2 + 2gx = \frac{\varepsilon_{eff}}{\varepsilon_r}S^2 - \frac{\sqrt{\varepsilon_{eff}}}{\sqrt{\varepsilon_r}}2gs. \qquad (3.11)$$

After algebraic manipulation, (3.9) and (3.11) give the following relation between s and η:

$$as^2 + bs + c = 0 \qquad (3.12)$$

where

$$a = \left[1 - \frac{1}{\varepsilon_r}\eta^2 - \left(\frac{(g-1)}{(g-a_0)}\right)^2\right]\frac{\varepsilon_{eff}}{\varepsilon_r},$$

$$b = \left[2g\left(\frac{(g-1)}{(g-a_0)}\right) - \frac{(g-1)}{(g-a_0)^2}\frac{1}{\varepsilon_r}{b_0}^2\eta^2 + \frac{1}{\varepsilon_r}2\eta^2 - 2g\right]\frac{\varepsilon_{eff}}{\varepsilon_r}$$

and

$$c = \left[\frac{1}{\varepsilon_r}\frac{g{b_0}^2\eta^2}{(g-a_0)} - \frac{1}{{\varepsilon_r}^2}\frac{{b_0}^4\eta^4}{4(g-a_0)^2} - \frac{1}{\varepsilon_r}\eta^2\right].$$

For fixed values of design parameters, α and g, s can be computed as a function of η from (3.12). These values of S and η are substituted into (3.8) and (3.11) to determine x and y, completing the solution for the lens design [1].

3.1.2.2 Rotman Lens MATLAB Simulation

In the previous section, we studied how the Rotman lens contour could be constructed based on geometrical optics. The arrangement of the beam port curve (input curve) and array port curve (output curve) was illustrated and relevant equations were extracted. In this section, we will simulate the geometrical equations and compute them using MATLAB.

The Rotman lens design equations have been incorporated into an intuitive code named RL_DESIGN. Implemented in MATLAB, RL_DESIGN features the full set of equations elaborated in the previous section and facilitates rapid and initial design of a Rotman lens for a particular set of initial parameters. The code permits the user to set the initial values for center frequency, scan angle (α), focal

length (F), focal ration (g), beam ports, array ports, element spacing and transmission line length. We considered several cases with different values to show the potential of our code (Figure 3-4).

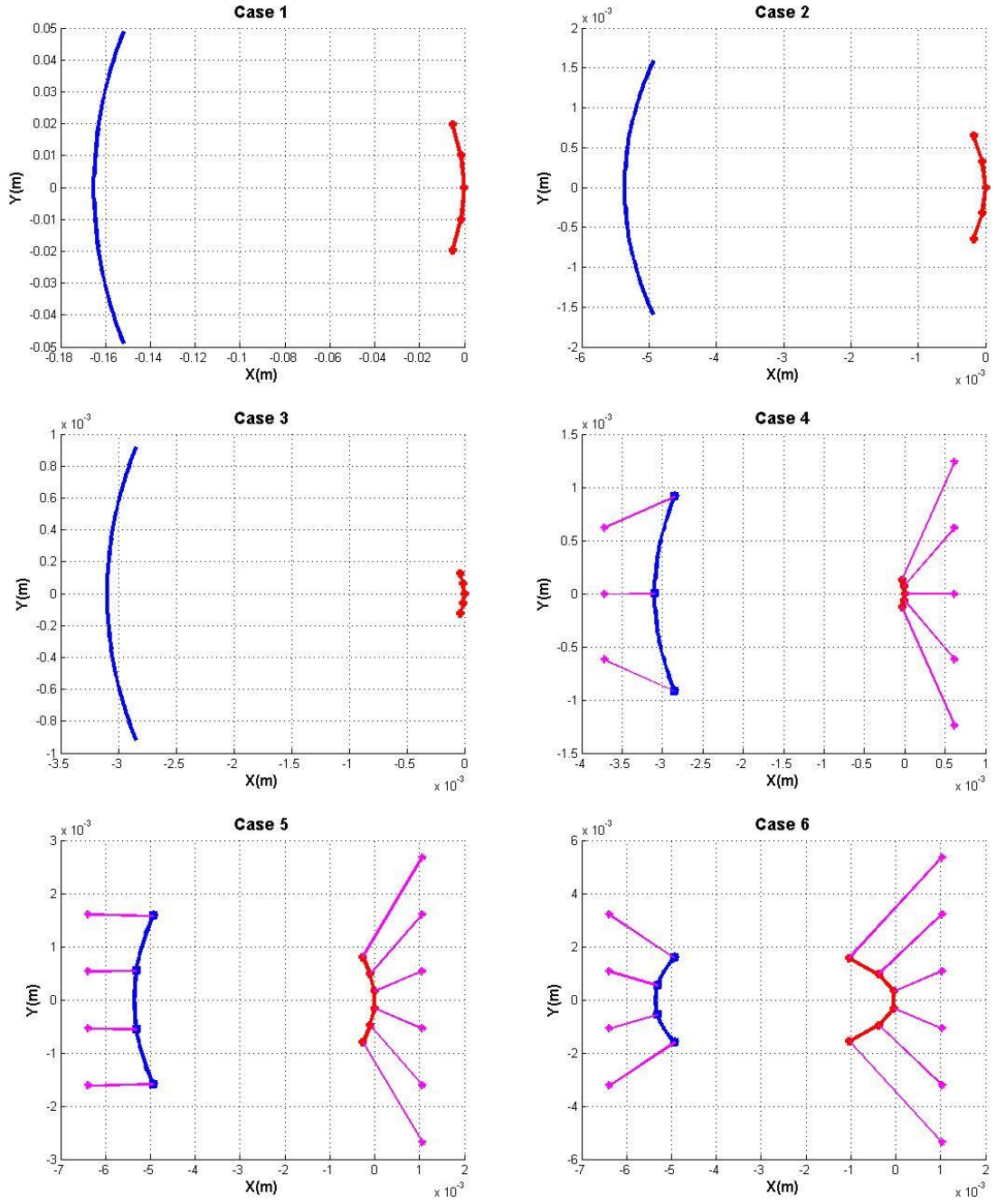

Figure 3-4 Rotman lens MATLAB simulation

Table 3-2 MATLAB Simulation Comparison: First case

	Case 1	Case 2	Case 3	Common Parameters
Frequency (GHz)	2.5	77	77	$\alpha = 30°$,F=2.5λ ,g=1.1
Permittivity	3.3	3.3	9.9	

Table 3-3MATLAB Simulation Comparison: Second case

	Case 4	Case 5	Case 6	Common Parameters
# Input/Output	3/5	4/6	4/6	$\alpha = 30°$,F=2.5λ ,g=1.1
Permittivity	9.9	3.3	3.3	Frequency=77GHz
Element spacing	0.5 λ	0.5 λ	λ	TL length=0.5 λ

3.1.3 Rotman Lens Design and Performance Simulation

In this section, we use Rotman lens designer (RLD) software from Remcom to design a Rotman lens and then simulate it using 2D (Momentum, Sonnet) and 3D tools (HFSS). Note that we are presenting simulations performed using HFSS for summarization purposes. The Rotman lens designer is a tool for the design, synthesis, and analysis of Rotman lenses and their variants. It is based on geometrical optics combined with classical Rotman lens design equations. It is intended for the rapid development and analysis of Rotman lenses, given several physical and electrical input parameters. Along with generating the proper lens contours, transmission line geometry and absorptive port (dummy port) geometry, RLD provides an approximate analysis of performance and generates geometry files. Using RLD, the lens type can be either microstrip or strip line [18].

3.1.3.1 Rotman Lens Designed at 2.5 GHz

The design is completed in three steps: Physical properties (geometry, lens type, focal contour shape, substrate and metallization); electrical properties (central frequency, bandwidth, element spacing, scan angle, array contour, beam contour and sidewalls), and transmission line properties (routed, straight, and array/beam/dummy ports transmission lines).

In our case, the microwave lens is designed to be a 3x5 element: it has 3 beam ports, 5 array ports suitable for a 5-element antenna array, and a centre frequency of 2.5 GHz with a 300 MHz bandwidth. It features a maximum scan angle of 20° and an element spacing of 0.5 wavelength. The lens is designed to be fabricated on a Rogers substrate with a dielectric constant of 2.2, a loss tangent of 0.0018, a thickness of 1.54 mm, and a 50 Ω impedance transmission. The tool predicts a size of 65x59 cm in the case of using microstrip.

The Rotman lens has an elliptical curvature and dummy ports in order to reduce reflections and thus increase the performance of the lens. The line routing geometry is sketched in such a way to ensure there is no overlapping and proper spacing is maintained between the lines.

Once the initial synthesis is finished, we export the lens for more advanced simulations. To do so, we use Momentum and SONNET as 2D tools, and HFSS as a 3D tool. However, for summary purposes, we will limit the discussion to HFSS simulations.

As mentioned in previous sections (Chapter 2), RL is a true time-delay beam-former, so we expect to see a constant phase shift with acceptable amplitude level at the output array. In the case of port 1, we can see that while the angle is not constant throughout the bandwidth, the general characteristic of Figure 3-5.b fits the conclusion. Furthermore, the received energy of ports is about -10 dB (Figure 3-5.c) and some of it is absorbed by the dumpy ports. However, this is acceptable to compensate for the reflection, which is less than -21 dB in the case of port1 (Figure 3-5.a).

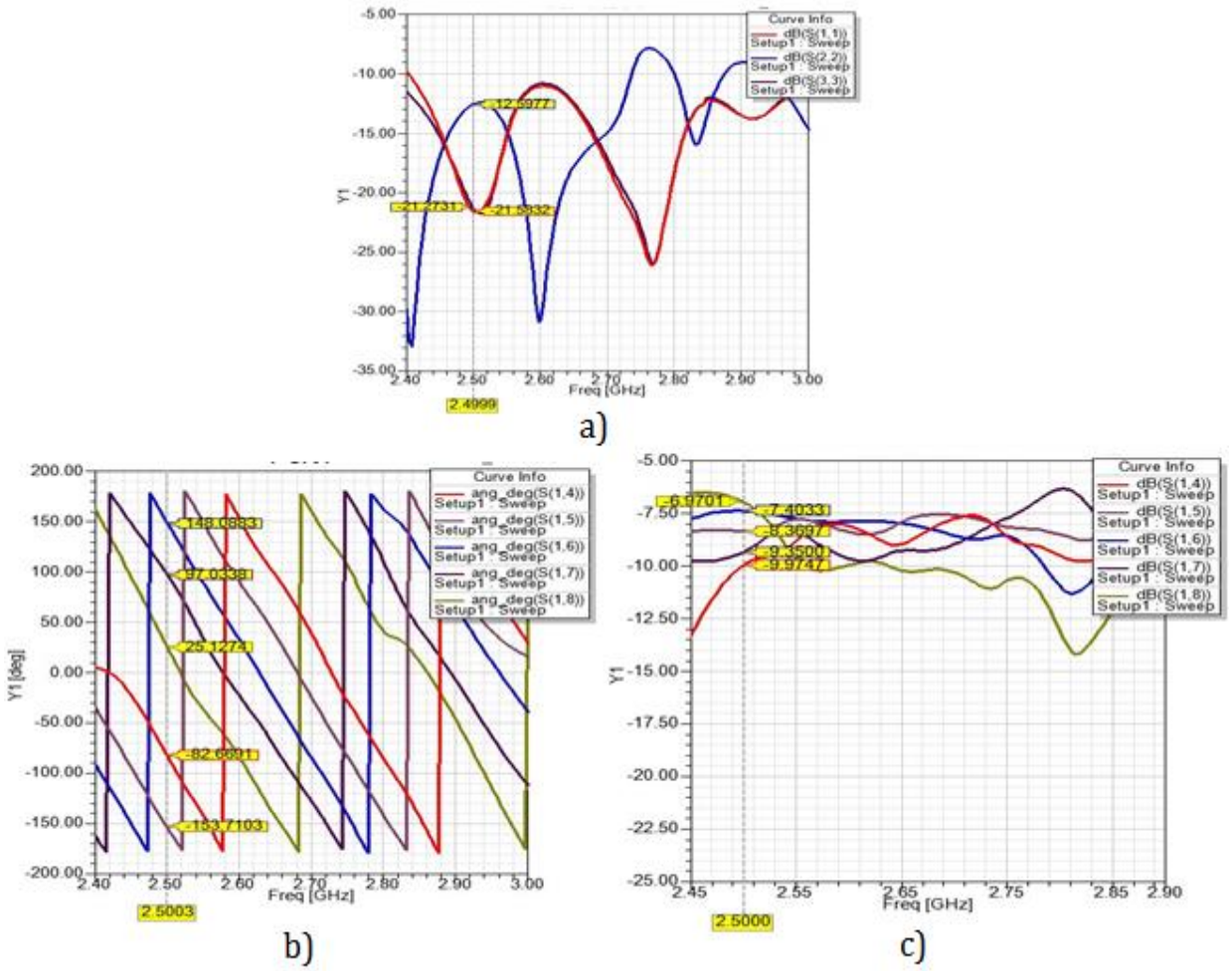

Figure 3-5 Simulations for microstrip RL at 2.5 GHz; a) return loss; b) and c) phase and S parameters for port 1

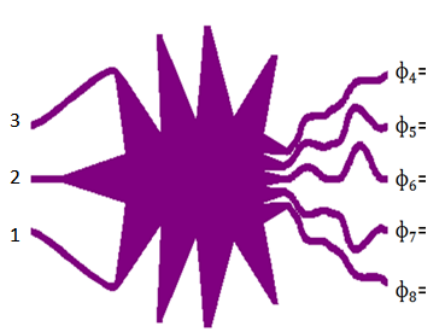

	PORT 1	PORT 3	PORT 2
ϕ_4=	-82°	25°	-95°
ϕ_5=	-153°	97°	-101°
ϕ_6=	148°	148°	-108°
ϕ_7=	97°	-153°	-101°
ϕ_8=	25°	-82°	-95°

Figure 3-6 HFSS results for microstrip RL at 2.5 GHz with a dielectric constant of 2.2

To understand the impact of the dielectric constant, we designed a Rotman lens that had the same characteristics but with a 9.9 permittivity. As can be seen, the general performance of the lens deteriorates in terms of reflection and phase shift (Figure 3-7). An acceptable behavior of the lens is between 2.6 GHz and 2.8 GHz only [17, 29].

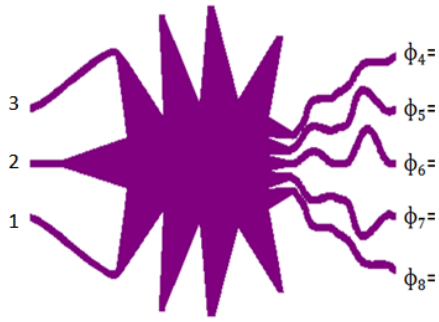

	PORT 1	PORT 3	PORT 2
ϕ_4=	108°	-166°	-3°
ϕ_5=	52°	-59°	-3°
ϕ_6=	-12°	-12°	10°
ϕ_7=	-59°	52°	-3°
ϕ_8=	-166°	108°	-3°

Figure 3-7HFSS results for microstrip RL at 2.5 GHz with a dielectric constant of 9.9

3.1.3.2 Rotman Lens Designed at 77 GHz

We employed the same design for two substrates. The first is an Alumna substrate, with a dielectric constant of 9.9, a loss tangent of 0.0002, a thickness of 25 mils (0.635 mm), and a 50 Ω impedance transmission. The second one is a Rogers substrate, with a dielectric constant of 2.2, a loss tangent of 0.0018, but with the same thickness and impedance as the first substrate.

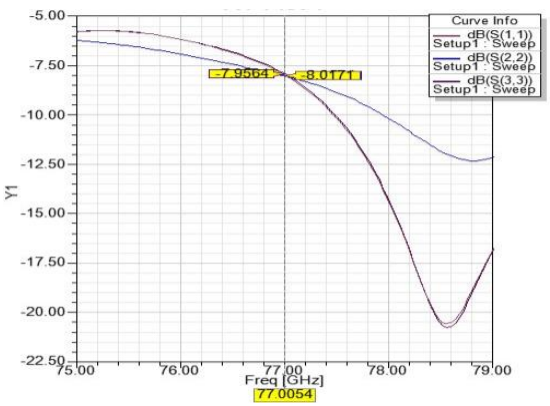

a)

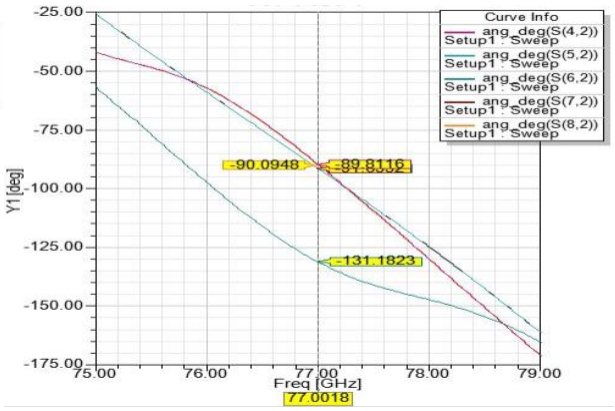

b)

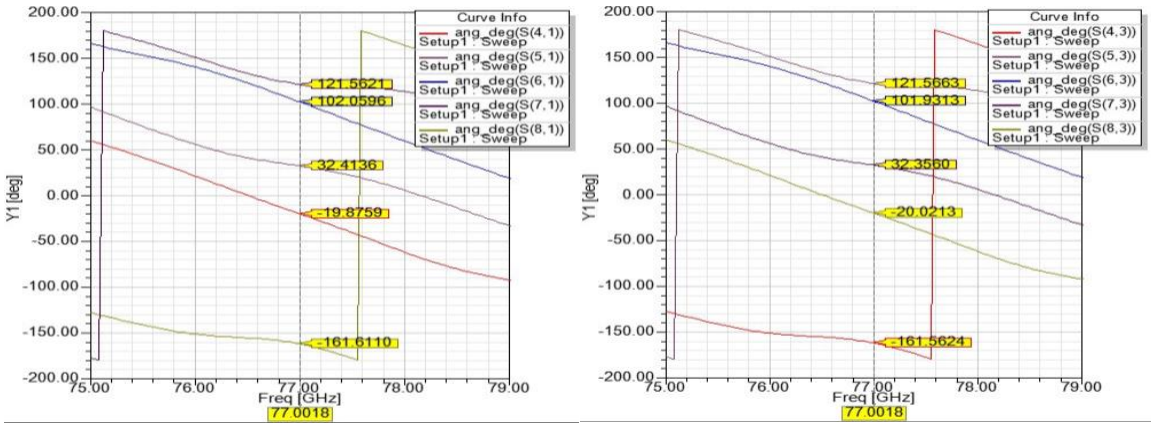

c) d)

Figure 3-8 RL with a dielectric constant of 2.2; a) return loss; b) phase for port 2; c) phase for port 1; d) phase for port 3

In the case of the dielectric with 2.2 (Figure 3-8), we note the expected behavior in terms of a phase shift with a reflection of -8 dB. The symmetry between port 1 and port 3 is verified in this case as well. In the case of 9.9, we note the same deterioration in the behavior of the lens in terms of the expected bandwidth and the shift in frequency. At this point, and in order to get an efficient RL at 77 GHz, we need to regenerate another design using an RLD of around 74, 75, 78 and 79 GHz. HFSS simulation of around 77 GHz results in the best-case scenario and is summarized in Figure 3-9.

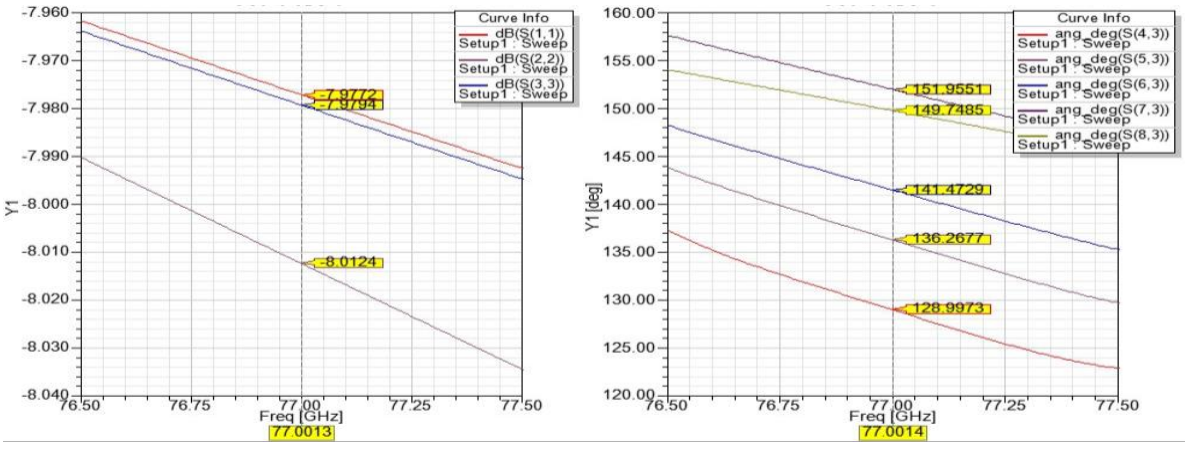

a) b)

Figure 3-9RL with a dielectric constant of 9.9; a) return loss; b) S parameters (phase) for port 3

3.1.4 Fabrication and Measurement of the Proposed Rotman Lens

A 3x3 Rotman lens structure was fabricated at the CIRFE lab and measured at the CIARS facility at 77 GHz. The fabrication was done in a single gold layer (Figure 3-10), and an absorber was used to emulate the effect of a 50Ω matching. The next sections show measurements in diverse scenarios, such as the absorber and probe position effect. At the end, a measurement vs. simulation study is presented.

Figure 3-10 Rotman lens measurements at 77 GHz

3.1.4.1 Measurements for the absorber effect

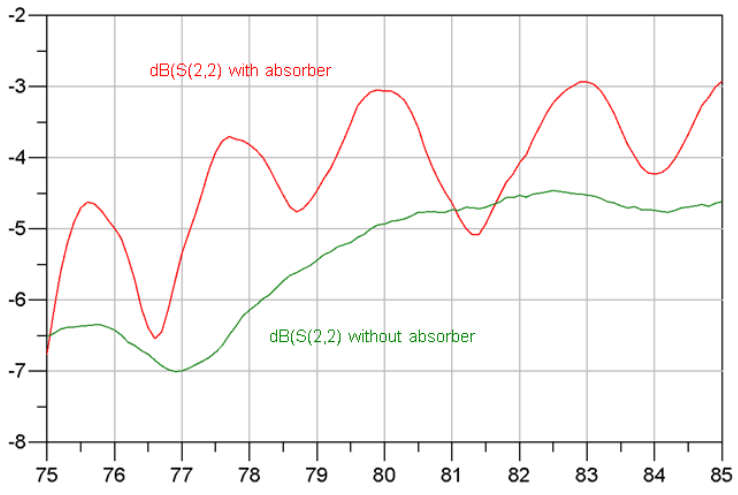

Figure 3-11 RL for port 2 absorber vs. without absorber

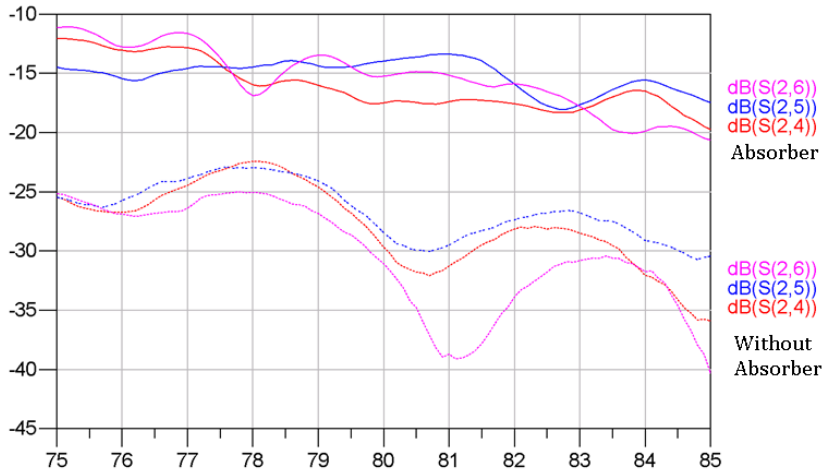

Figure 3-12 IL for port 2 absorber vs. without absorber

We can conclude that the absorber plays the role of a matching termination. It is useful in instances where we have a structure with multiple terminations, such as the case at hand. Here, we have to terminate four ports at a time if we are doing two port measurements.

3.1.4.2 Measurements for the probe position effect

In this section, we present the effect of probe positioning while measuring at 77 GHz. The difference between contact position A and contact position B is a few microns.

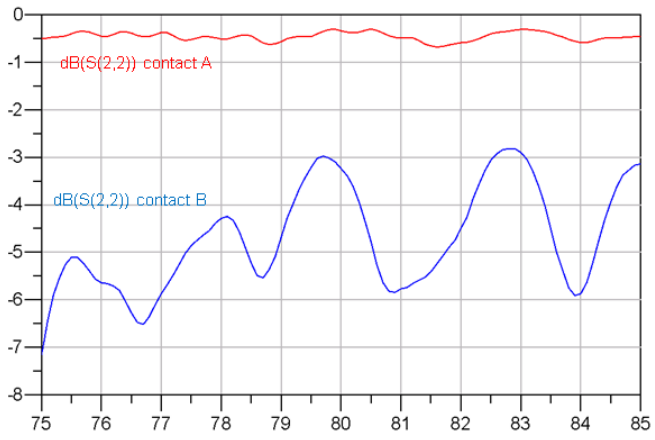

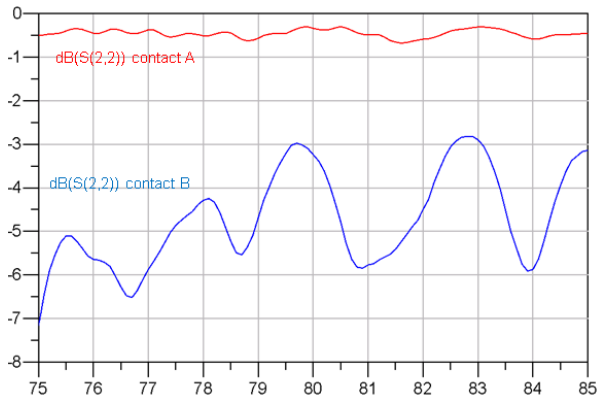

Figure 3-13vRL (top) and IL (bottom) showing contact A vs. contact B effect

3.1.4.3 Simulation vs. measurement results

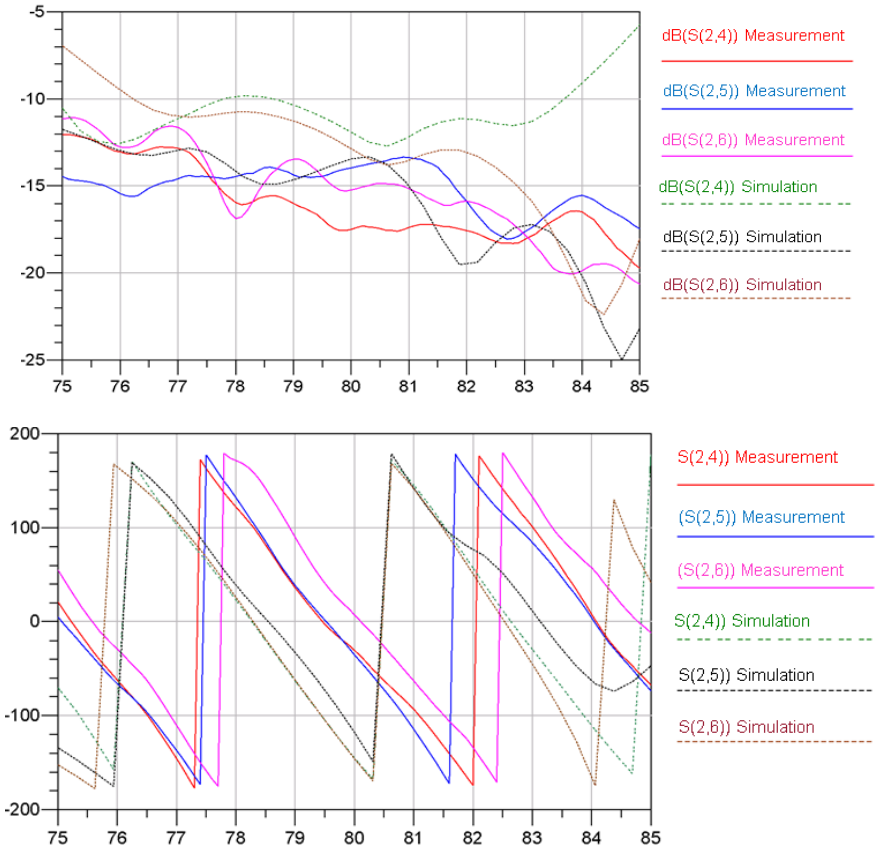

Figure 3-14 IL (top) and phases (bottom) for port 2

The experimental results present the behavior of a Rotman lens. There is a shift in values between the simulations and the experimental results due to the high sensitivity towards length. Hence, a small shift in landing the probe can result in a big difference in the S parameters, as shown. We considered the experimental results that presented the same values from the same measurements at different times, which indicates the reputability in measurement. The simulation can coincide in terms of phases with the measurement, if we did several that consider small shifts in the distance of the lamped ports.

3.1.5 Beam-forming network using a Rotman lens

In this section, we propose a 2D structure integrating an SP3T MEMS switch. For this, we will employ RL as a beam-former and the patch antenna array that will be fabricated on a single Alumina wafer using the UW MEMS ISO process, which is a variation of the UW-MEMS standard process.

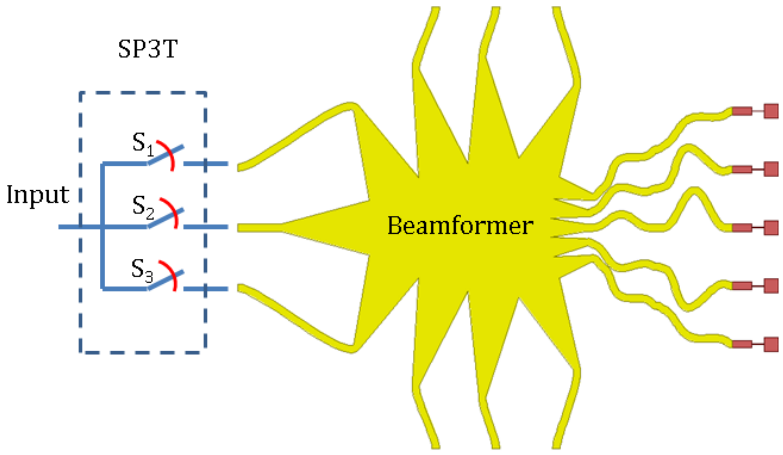

Figure 3-15 Complete structure including the switching, Rotman lens, and the antenna array

As a proof of concept, we simulate a BFN at 2.5 GHz. The BFN contains a Rotman lens and a network of patch antenna (with a single antenna per output). A scanning angle of -10°, 0 and +10° is reached once we excite successively through port 1, port 2, and port 3.

The radiation pattern in this case is presented in Figure 3-16.

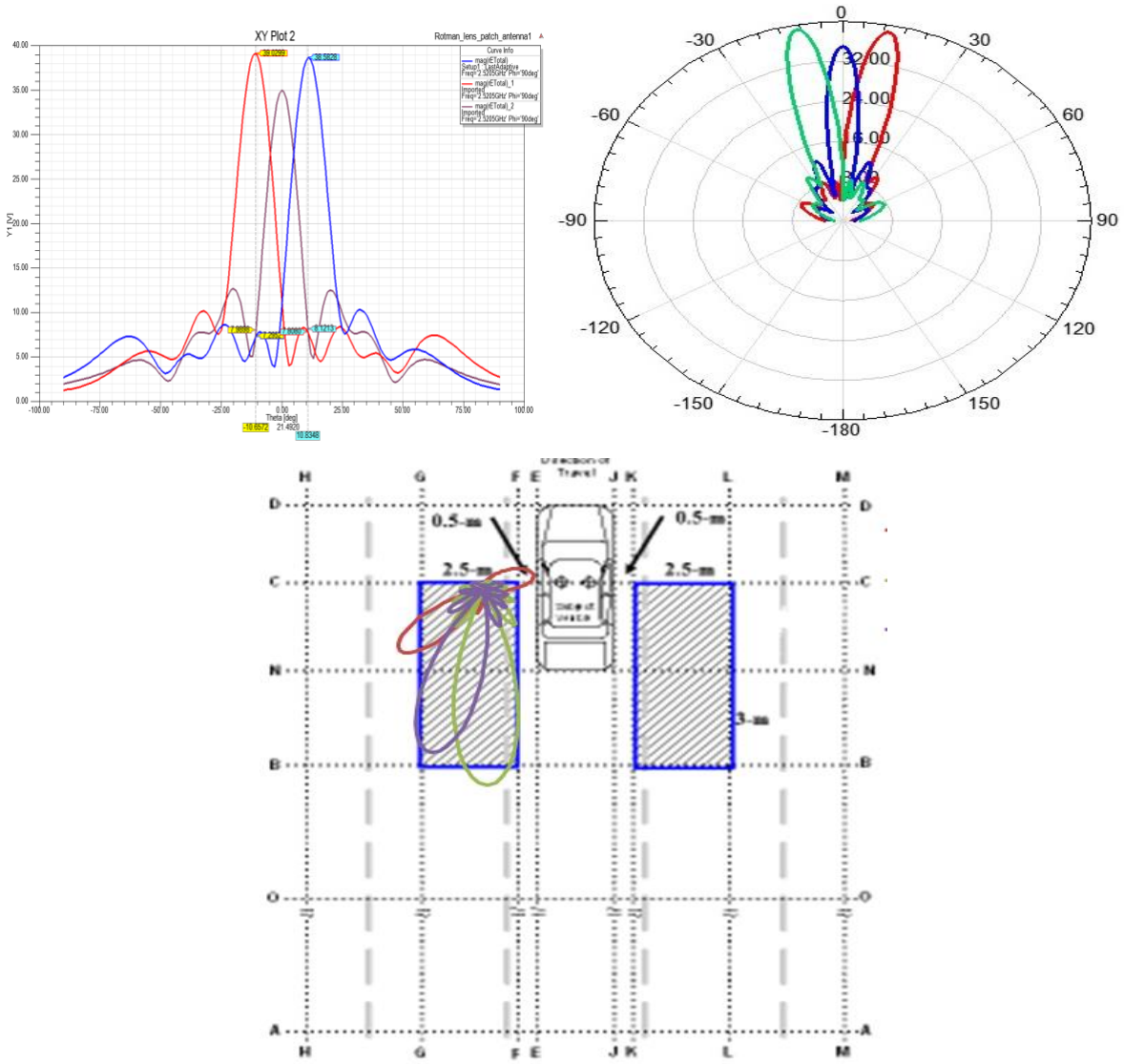

Figure 3-16 Radiation pattern at 2.5 GH and conformal to type I radar

3.2 RF MEMS Switches

3.2.1 General Specifications

To date, according to contact styles, two main types of switches have been developed: metal-to-metal contact switches, and capacitive contact. Capacitive switches are chosen because their large contact area can handle more RF power than metal-to-metal contact switches.

According to actuation types, many thus far have been developed. These include electrostatic, thermal, magnetic and piezoelectric actuation. Electrostatic is chosen here due to its simplicity and low power consumption.

For mechanical structure, we have two main types: beam and cantilever. Beam is generally more advantageous than cantilever, since the bridge has a greater value of "intrinsic spring", and is more stable and less sensitive to stress [25, 47, 52].

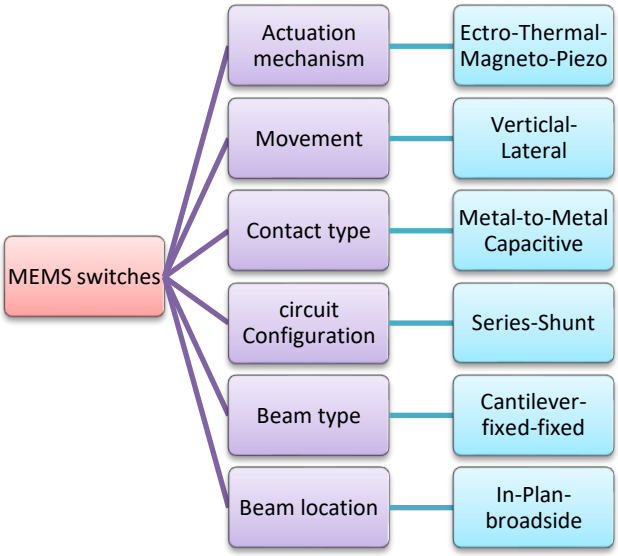

Figure 3-17 RF MEMS switch general specifications

3.2.2 Typical Approach to Design 77 GHz Switch [3]

In this section, we present the typical approach to designing a 77 GHz MEMS switch. We start by briefly explaining the basic electromechanical and electromagnetic notions of the RF MEMS switch.

3.2.2.1 Electromechanical Modeling

The principle of switching is applying voltage bias between the bottom electrode and the beam. Equations (3.13) and (3.14) show the relationship between the electrostatic and mechanical factors when there is no RF signal involved.

$$V_{Pull-Down} = \sqrt{\frac{8Kg_0{}^3}{27\varepsilon_0 A_{DC}}} \tag{3.13}$$

$V_{Pull-Down}$ is the minimum electrostatic voltage that results in the collapse of the beam to the down-state position. A_{DC} is the DC area, ε_0 is the permittivity of air, K is the spring constant, and g_0 is the zero-bias bridge height.

$$V_{Hold-Down-DC} = \sqrt{\frac{2Kg_0}{\varepsilon_0 A_{DC}}\left(\frac{t_d}{\varepsilon_r}\right)^2} \tag{3.14}$$

For the switch to stay in the down-state position, the electrostatic force must be larger than the mechanical restoring force. This is achieved for hold-down-DC voltage $V_{hold-Down-DC}$, where t_d is the dielectric thickness and ε_r is the dielectric permittivity.

3.2.2.2 Electromagnetic Modeling

The switch device may fail to operate properly due to an incident RF signal of a power P. The two types of failures are RF self-actuation and RF latching. RF self-actuation occurs when the RF power creates the potential to pull the switch into the down-state position without applying a DC bias. RF latching occurs when the input RF power generates a force that keeps the switch down even when the DC bias applied is removed.

The electromagnetic modeling takes in account the circuit configuration. Below, we present the formulas for both series and shunt cases.

Equations (3.15) and (3.16) illustrate, respectively, RF self-actuation and RF latching.

$$V_{DC-eq} = \sqrt{\frac{A_{RF}}{A_{DC}}}V_S = \sqrt{\frac{A_{RF}}{A_{DC}}}\frac{V_{max}}{\sqrt{2}} = \sqrt{\frac{A_{RF}}{A_{DC}}}\sqrt{PZ_0}\ (shunt)$$

$$V_{DC-eq} = 2\sqrt{\frac{A_{RF}}{A_{DC}}}\sqrt{PZ_0}\ (series) \tag{3.15}$$

where V_{DC-eq} (the equivalent DC voltage due to the RF) is power on the line, Z_0 is the characteristic impedance of the CPW line, and A_{RF} is the RF area.

$$V_{Hold-Down-RF} = \frac{2\sqrt{2PZ_0}}{\omega c_d Z_0\sqrt{2}}\frac{A_{DC}}{A_{RF}} = \frac{\sqrt{2PZ_0}}{\pi f c_d Z_0\sqrt{2}}\frac{A_{DC}}{A_{RF}}\ (shunt)$$

$$V_{Hold-Down-RF} = \frac{\sqrt{2PZ_0}}{\omega c_d Z_0 \sqrt{2}} \frac{A_{DC}}{A_{RF}} = \frac{\sqrt{2PZ_0}}{2\pi f c_d Z_0 \sqrt{2}} \frac{A_{DC}}{A_{RF}} \quad (series) \tag{3.16}$$

where C_d (the down-state) is position capacitance and f is frequency.

3.2.2.3 Shunt vs. Series

The choice of the structure will be based on performance criteria. The chosen topology allows us to maximize the power handling, avoid RF self-actuation and RF latching, and minimize the switching time. The circuit configuration affects the value of the power. When the switch is in the up-state position, there is a risk of an auto-activation. We can conclude that

$$P_{Shunt_{Up-state}} = 4P_{Series_{Up-state}} \tag{3.17}$$

At the same time, however, when the switch is in the down-state position, there is a risk of latching. So, we can see that

$$P_{Shunt_{Down-state}} = \frac{1}{4} P_{Series_{Down-state}} \tag{3.18}$$

Thus, the shunt configuration is advantageous in the up-state position, while the series configuration is advantageous in the down-state position. However, we must reason otherwise in order to conclude. In fact, to maximize power handling, we have to minimize both $V_{DC-equivalent}$ and $V_{Hold-Down-RF}$. $V_{Hold-Down-RF}$, as shown in (3.18), depends on the frequency. Therefore, it is possible to minimize it by increasing the frequency [3, 22, 37].

3.2.2.4 Typical Approach to Modeling a MEMS Switch in W-band

The typical approach to modeling a W-band switch is based on the extraction of the equivalent capacitance area from the equations relating the electrical model and S-parameters. We will start by briefly presenting the equivalent circuit in both the series and shunt topology cases.

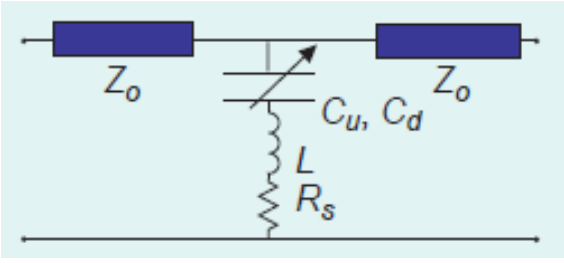

Figure 3-18 RLC model for typical capacitive shunt switch

In the case of a MEMS series switch, the RLC model is a series capacitance in the up-state position and a small resistance in the down-state position. The isolation of a series switch in the up-state position is given by

$$|S_{21}|^2 = 4\omega^2 C_u^2 Z_0^2$$

where C_u is the up-state capacitance and Z_0 is the transmission-line impedance. The insertion loss is

$$|S_{21}|^2 = 1 - \frac{R_s}{Z_0}$$

where R_s the contact resistance of the switch.

In the case of shunt-capacitive switch (Figure 3-18), the electrical model of the up-state reflection coefficient is

$$|S_{11}|^2 = \frac{\omega^2 C_u^2 Z_0^2}{4}$$

where C_u is the up-state capacitance of the switch.

The down-state isolation formula is

$$|S_{21}|^2 \cong \begin{cases} \frac{4}{\omega^2 C_d^2 Z_0^2} & for\ f \ll f_0 \\ \frac{\omega^2 C_d^2 Z_0^2}{4} & for\ f = f_0 \\ \frac{4\omega^2 L^2}{Z_0^2} & for\ f \gg f_0 \end{cases} \qquad \text{where } f_0 = 1/(2\pi\sqrt{LC_d}) \qquad (3.19)$$

Therefore, by knowing the operating frequency and the S-parameters value expected, computing the value of the capacitance is relatively straightforward. Once we have the typical capacitance area dimensions, we can design the switch based on technology specifications (transmission line, gap, switch width), fringing capacitance, electrode dimensions, line impedance, etc. After simulations and tuning the switch dimensions, we typically end up designing a matching network, either a T-match or π-match, to compensate for the high up-state capacitance and high reflection losses [36, 51].

3.3 Surface Micromachined Planar Structure Design Using UW-MEMS

This section presents an SP3T structure simulated using HFSS and conformal to the design of a typical UW-MEMS process [59]. The structure is entirely symmetrical, so any branch can be used as an input/output. During the OFF state, all the cantilevers are at rest and the input signal would not be able to pass through. During the ON state, actuating the input and one of the outputs would push the affected cantilevers to the down position and touch the central plate. The RF signal would also get through the

chosen path. At 77 Ghz, in the OFF state, we get a return loss of -1.6db and the worst insertion loss is -23db. In the ON state, we get an IL of -17db, an isolation of -0.9 db, and an RL of -14db.

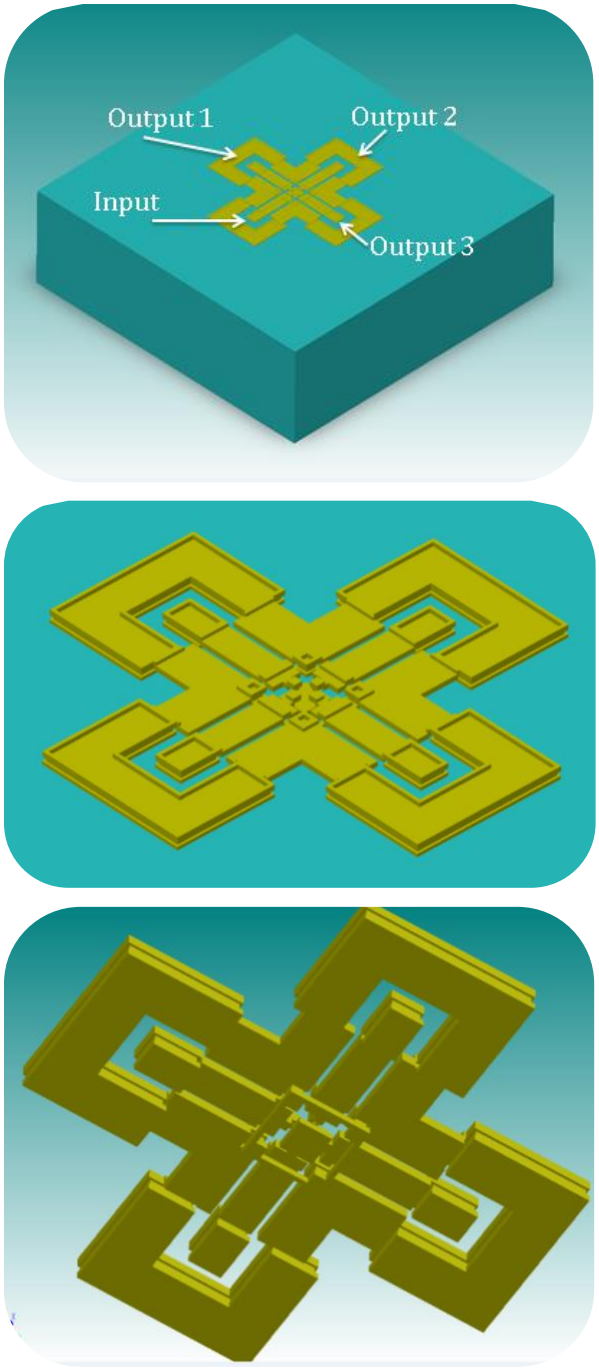

Figure 3-19 Proposed SP3T structure

3.3.1 Surface Micromachined Planar Structure Design Using UW-MEMS ISO

This section will describe the main steps required for the fabrication of the proposed SPST 77 GHz series contact switches as well as the SP3T (or, generally, SPNT) switches based on the same architecture. Because the beam-former and patch antenna are planar, we will use the G1 layer of the process to implement them, and we do not need to show them when describing the developed process. A cross-section of the proposed RF MEMS series switch at 77 GHz is presented in Figure 3-20.

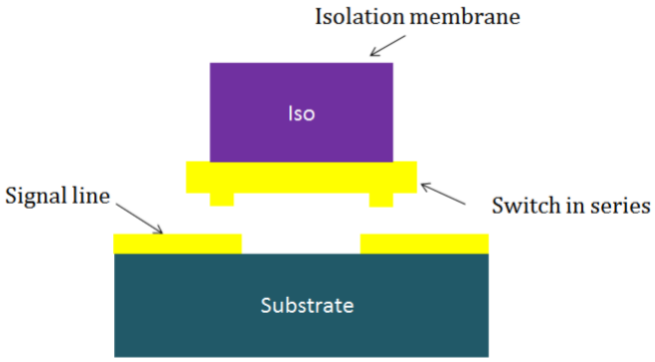

Figure 3-20 Cross-section of the proposed architecture of the 77 GHz series contact switch

Figure 3-21 shows a 3D version of the proposed architecture for the 77 GHz series contact switch based on planar transmission lines. The conducting material is gold, similar to the standard UWMEMS process [54]. The switch is 160x30x1 µm, and the CPW is a 12/30/12 µm 50Ω transmission line at 77 GHz.

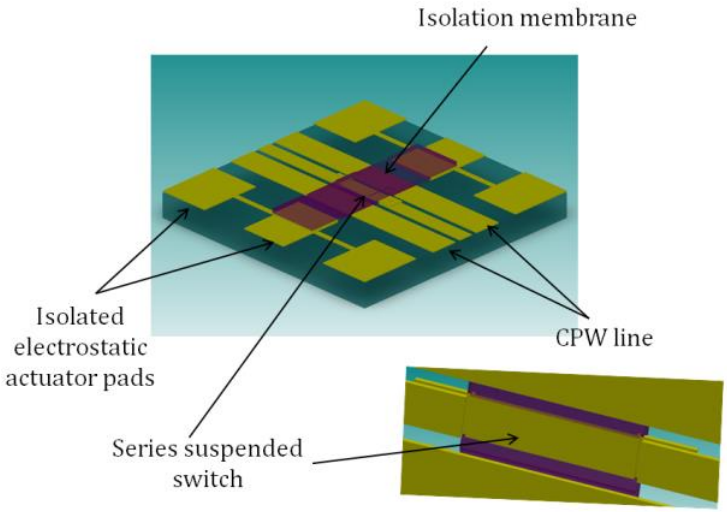

Figure 3-21 Proposed architecture for the 77 GHz series contact switch

The switch is in series, has two dimples, and is suspended because it is attached to the isolation membrane. Applying a voltage via the electrostatic actuator would bring the membrane down and the switch would follow in the ON state. Figure 3-23 shows how the membrane is suspended at the electrostatic actuator level.

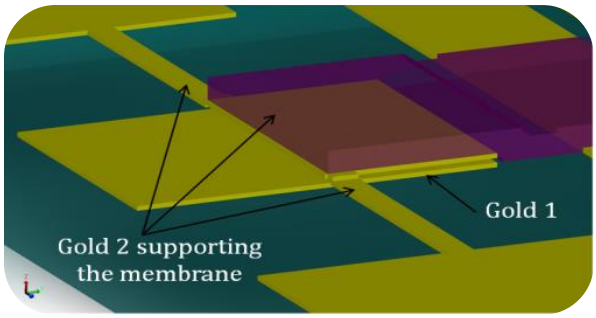

Figure 3-22 Isolation membrane suspended by Gold 2; electrostatic actuation between Gold 1 and Gold 2

Table 3.4 details the main microfabrication process for the proposed switch, which we refer to as UWMEMS-ISO.

Table 3-4 Main Microfabrication Steps of the UWMEMS-ISO Process

#1	Step	Mask	Material	Thickness
0	Cleaning of wafers	N.A.	N.A.	N.A.
	Description: The wafers are 2.5" square 10mils Al2O3 substrates with a relative permittivity of 9.9 and a loss tangent in the range of 2 x 10-4 . The cleaning of wafers is based on RCA.			
1	1st gold layer	G1: LF	+ Cr + Au + Au	+ 50 nm + 50 nm + 1 µm
	Description: Cr is used as an adhesion layer for Au, but Ti, TiW, etc., can also be used. The thin 50nm Au is used as a seed layer for the electroplated thick Au on top of it. Together with the G2 Au layer, this layer is used for building planar transmission lines, electrodes for electrostatic actuation, and current loops for electromagnetic actuation. This layer will be used to implement the beam-former (Rotman lens) and array of patch antennas.			

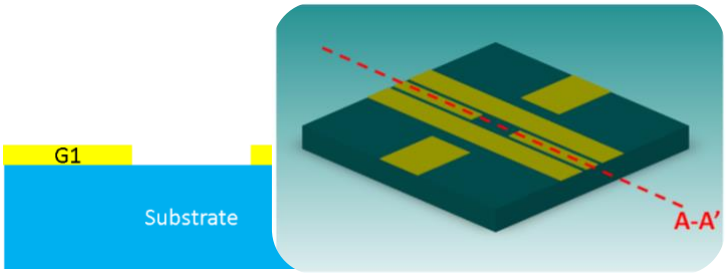

2	Sacrificial layer	N.A.	+ SiO2	+ 2.0 µm

Description:

Ti is used as an adhesion layer between SiO2 and Au.

The sacrificial layer thickness defines the air gap for the actuators.

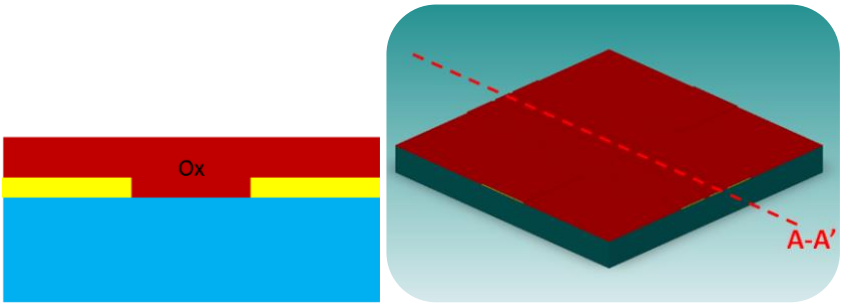

3	Dimple	D: DF	- SiO2	- 0.5 µm

Description:

The dimple pattern defines mainly where the electrical Au-Au contact is to occur for switching applications.

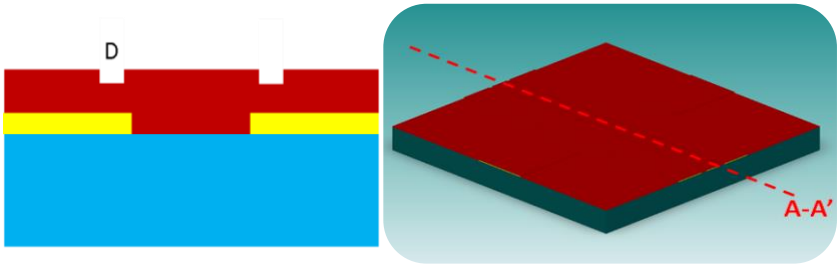

5	2nd Gold Layer	G2: LF	+ Au	+ 1.0 µm
	Description: The second gold layer is to be suspended for the fabrication of switching contacts. It is also used to fabricate the suspended parts of the actuators (plates for electrostatic actuation, current loops for electromagnetic actuation, and beams for thermal actuation). 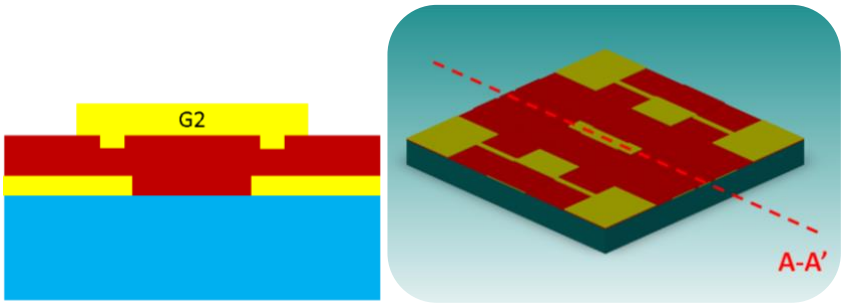			
6	Isolation Membrane	Iso: LF	+ PI	+ 10.0 µm
	Description: The isolation membrane serves mainly as an insulating structural layer for switching; it can be either SU8 or nitride. Isolated electrostatic and/or electromagnetic actuators can be built using that membrane. Additionally, the membrane can be used to implement bimorph structures with the 2nd gold layer. 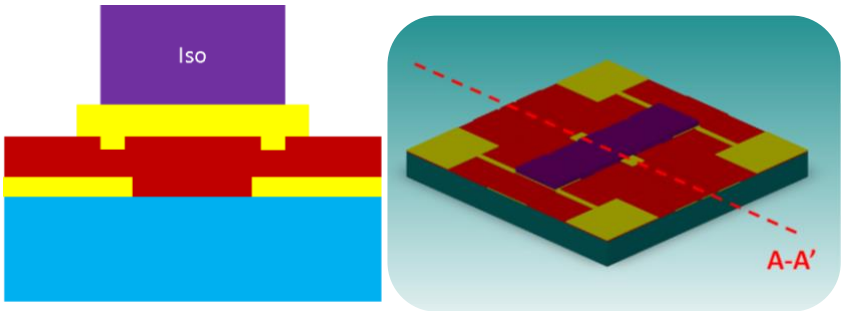			
7	Release	N.A.	N.A.	N.A.
	Description:			

	Devices are wet-released in buffered HF (BHF), then rinsed in water and isopropyl alcohol (IPA), and eventually placed into fresh IPA in the critical point drier (CPD) system to finalize the release process. 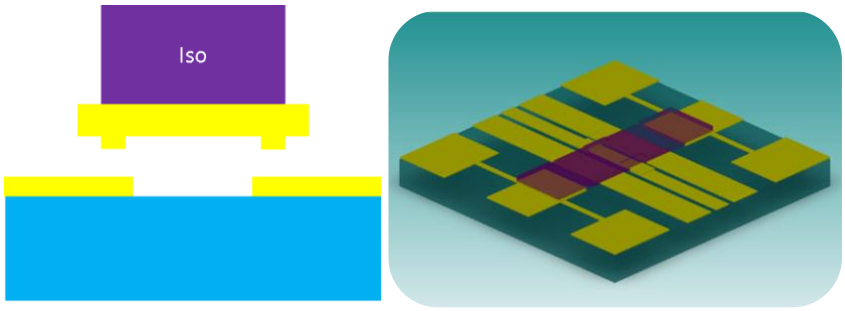
#1: main step index, LF: light field, DF: dark field, PI: polyimide	

In the mm-Wave range, metal thickness is not critical due to the relatively thin skin depth; however, surface roughness is a critical parameter. Substrate thickness is also a critical parameter in the design of high frequency switches. Reducing the thickness of the substrate (e.g., from 25mils to 10mils Alumina substrate in the UWMEMS process) allows for increased suppression of the substrate modes and an acceptable return loss when the switch is OFF.

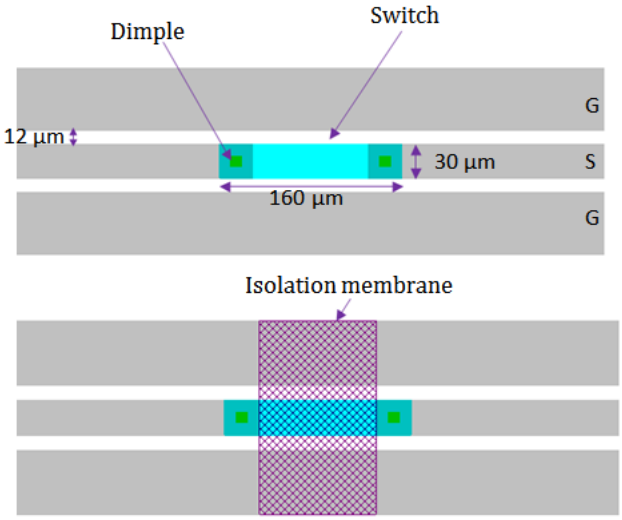

Figure 3-23 Isolation membrane suspended by Gold 2; electrostatic actuation between Gold 1 and Gold 2.

The proposed structure was analyzed using HFSS and Sonnet simulation packages in terms of the electromagnetic performance. Figure 3-24 displays the results for insertion loss and return loss in both states of the switch in Sonnet.

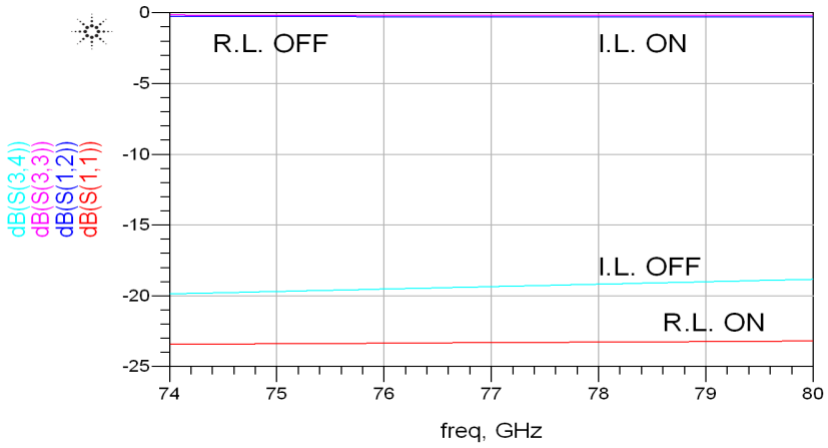

Figure 3-24 Electromagnetic simulation of insertion loss and return loss in both states of the proposed series contact switch in Sonnet

Three series-configured MEMS switches, based on the SPST switch already presented, have been used to construct the complete SP3T switch (Figure 3-25). The SP3T switch configuration is incomplete and essentially just a simple presentation of the SP3T. The length of the transmission lines should be established after a complete study and simulations. This switch is used to open or short the center conductor of the CPW line to the output port. When the series switch is actuated, the RF input signal passes to its port, whereas the RF signal is reflected away from the arm containing the non-actuated switch.

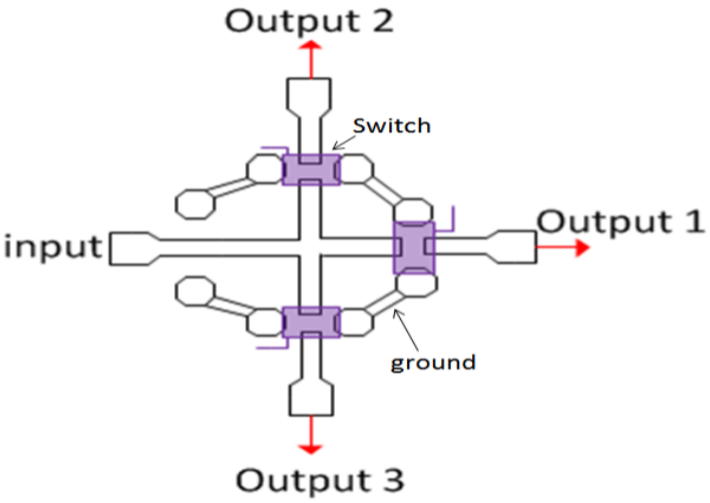

Figure 3-25 SP3T switch based on [47]

Chapter 4
3D Monolithic Beam-forming Network

One of the most serious limitations of high performance radar is beam-forming network systems. This limitation is due to the inherent complexity and bulkiness of the additional circuitry and hardware needed to implement multiple functionalities into a single complete system. As a result, producing radar systems requiring such complexities is often a challenge that comes at the price of increased size, weight, and cost [16].

In this chapter, we investigate several architectures that permit the integration of the front-end radar system in a single chip, including a BFN employing RL realized in SIW technology on a high dielectric constant substrate, and a 3D monolithically integrated BFN on a silicon substrate employing MEMS-based waveguide switches, waveguide RL, and an antenna array.

4.1 High Dielectric Constant Material/Substrate Beam-former Development

High dielectric constant material silicon-based dielectrics (SiO2, Si3N4, SiOxNy, etc.) are widely used as the key dielectrics in the manufacturing of silicon integrated circuits (ICs) and virtually all other semiconductor devices. Dielectrics, which have a value of dielectric constant ε_r more than that of silicon nitride ($\varepsilon_r > 7$), are classified as high dielectric constant materials, while those with a value of ε_r less than the silicon dioxide ($\varepsilon_r < 3.9$) are classified as low dielectric constant materials.

Considering the option of high dielectric constant materials is interesting because it would tremendously miniaturize the structure of a Rotman lens. Theoretically, it would shrink the size of the lens by a factor of $\sqrt{\varepsilon_r}$. From that perspective, we could use them either as a material base or a substrate base for a beam-forming Rotman lens.

The design of a MEMS Rotman lens that uses a high dielectric constant PZT (Lead Zirconium Titanate, ε_r=1200) thick film to fill the lens cavity has been presented by [11]. The material was supposed to be deposited by Sol-gel, with the author claiming in the reference [11] that the structure would be fabricated; however, in his thesis, the author reported that the research team had declined to use that option because the structure would be extremely lossy. On the other hand, a high dielectric constant substrate (i.e., BLT ceramic with ε_r up to 170 [55]) can be used as a support to fabricate the Rotman structure. A promising candidate for developing this platform is substrate integrated waveguide (SIW) technology. SIWs are integrated waveguide-like structures fabricated by using two periodic rows of metallic vias or slots connecting the top and bottom ground planes of a dielectric substrate.

4.2 A Monolithic 3D Integrated BFN on a Silicon Substrate

4.2.1 Development of MEMS-based Waveguide Switch at 77GHz

Based on the sections entitled "Waveguide Switch Technologies" and "Waveguide-to-CPW Transitions" presented in Chapter 2, Figure 4-1 offers a basic schematic of the proposed DC-contact shunt MEMS waveguide switch based on the work of [5]. It consists of a ridge waveguide incorporated with MEMS actuators. The dimensions of the WR-10 ridge W-band waveguide are a=2.54 mm and b=1.27 mm. The ridge width and height are designed to leave a gap on the bottom side of the waveguide that consists of the length of the POLYMUPMS/MEMS switch. It is well-known that the electric field has a strong intensity in this gap along the ridge where the POLYMUMPS plates are located. When the plates are in the horizontal position, the switch is ON and the wave propagates through the waveguide. By moving the plate to the vertical position, wave propagation is blocked and the switch is OFF. In order to bias the switch, we add a DC line through the holes on the top wafer.

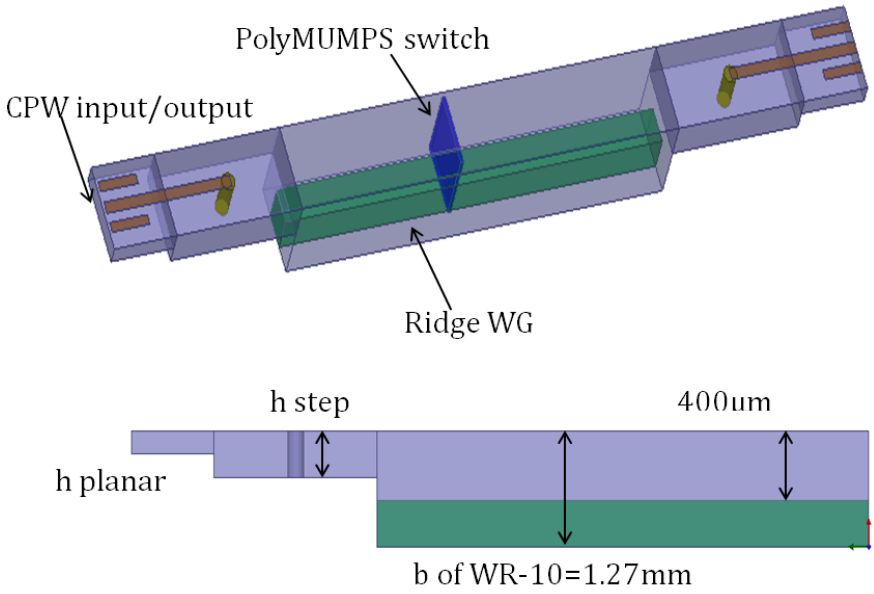

Figure 4-1 Proposed SIW Rotman lens on high dielectric constant substrate

4.2.2 Micromachined 3D MEMS-Waveguide Design Stage 1

A radar design compatible with this type of micromachining process is developed to fabricate a W-band high resolution radar structure with a microstrip patch array antenna.

4.2.2.1 Micromachined 3D structure overview

This section will present a comprehensive overview of the proposed structure:

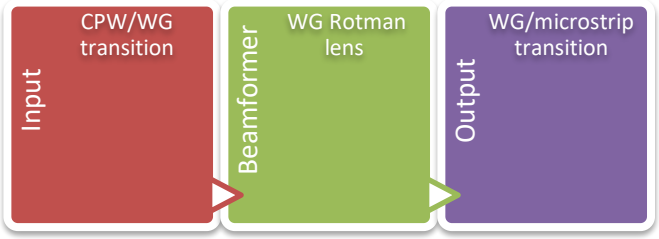

Figure 4-2 Top level of the proposed 3D structure

The micromachined structure is mainly waveguide, but the input and output are planar lines (CPW or microstrip). Hence, for this part of the structure, a waveguide-to-CPW line transition is proposed and developed in the next section.

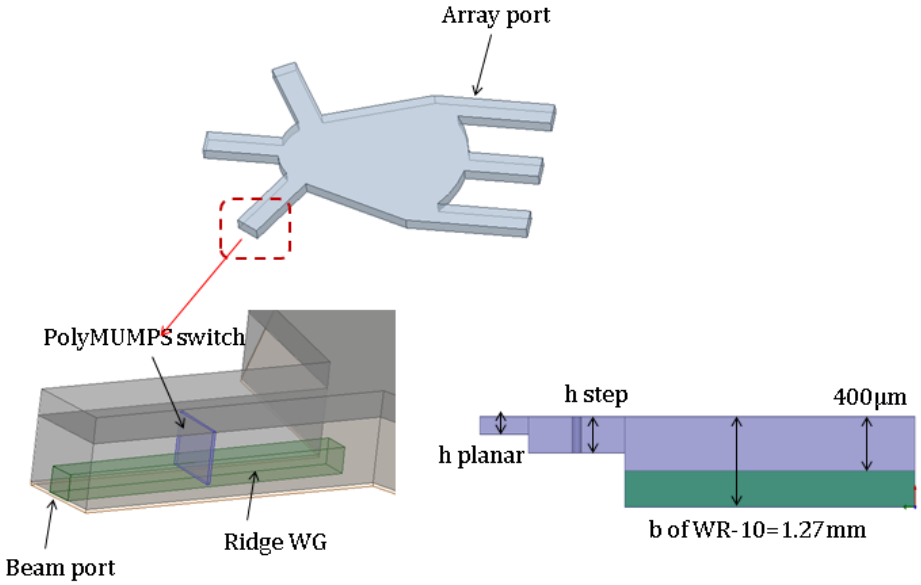

Figure 4-3 Micromachined 3D structure overview

As explained in Chapters 2 and 3, for the beam-forming network to perform, switching is required. Therefore, a PolyMUMPS switch is implemented.

At the output, the Rotman lens is connected to an array of antenna. The transition would thus permit us either to test the structure as it is without the antenna by landing two probes (one at the input and one at the output), or to connect the structure to a microstrip antenna array.

For the front-radar to function, as explained in Chapter 2, active electronics are needed. Thus, the integration of these chips in the process is suitable for achieving maximum integration and size control. In the next sections, we explain in detail every aspect of the design, after which we present the process in detail.

4.2.2.2 Fabrication Process

In this section, we present the microfabrication processes for realizing micromachined radar structures. As discussed, the passive components of the radar front-end (e.g., the antenna array, CPW-to-waveguide transition, and waveguide Rotman lens) are designed in such a way that they can be fabricated on the same wafer through the same series of microfabrication processes.

The fabrication of the micromachined radar components is performed on two silicon wafers. The waveguide and the multi-step for transition are realized on a "bottom wafer", with DRIE multi-step etching processes being used to realize these structures. The top cover for the waveguide-based structures, a suspended CPW line, and the antenna array are realized on a "top wafer". The two wafers – bottom and top – are then bonded using a gold-to-gold thermo-compression bonding technique to form the complete micromachined structure (Figure 4-4).

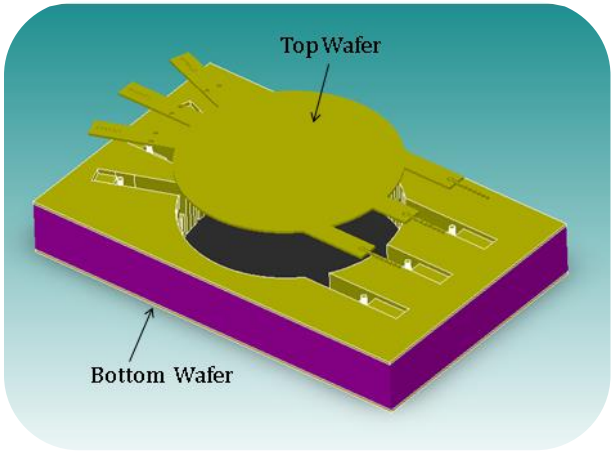

Figure 4-4 Final structure including top and bottom wafer

Table 4.1 and Table 4.2 detail the main microfabrication processes for the proposed 3D micromachined structure, based on the transition detailed in Chapter 2. The first table shows the steps for the bottom wafer, while the second table shows the steps for the top wafer. Because we need a thick silicon bottom wafer (thicker than "height b" of the WR-10 waveguide, which is 2.54x1.27mm), let us consider 2mm thick silicon (from SVM, for example).

Table 4-1 Main Microfabrication Steps of the Bottom Silicon Wafer

#1	Step	Mask	Material	Thickness
0	Cleaning of wafers	N.A.	N.A.	N.A.
	Description: The wafers are 2.5" square SVM silicon substrates with a relative permittivity of 11.68 and a loss tangent in the range of 10-4. The cleaning of wafers is based on RCA.			
1	Multi DRIE	4 L.F		
	Description: The DRIE method is a highly anisotropic etch process suitable for creating deep features with vertical walls in silicon substrates. The vertical structures are achieved through repetition of a two-phase cycle: 1) the standard plasma etch with SF6 flow, and 2) the deposition of a passivation layer with a flow of C4F8 gas. The standard method to create multi-step structures is to use multiple-masks, as described in [50]. In this method, to achieve an N-step structure, the wafer is patterned successively with N different mask layers. For our application, four different mask layers are used to realize three-step structures.			

Mask 1

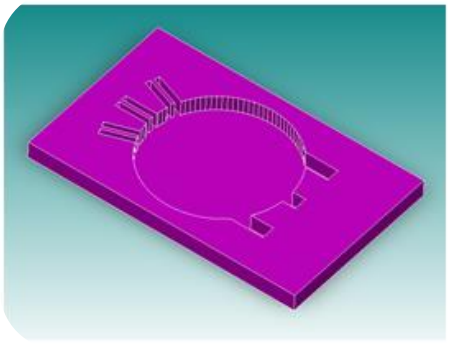

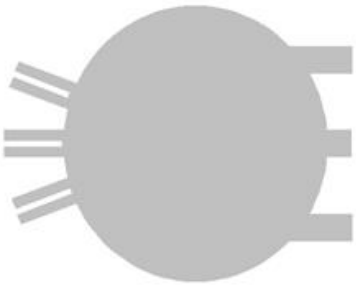

Mask 2

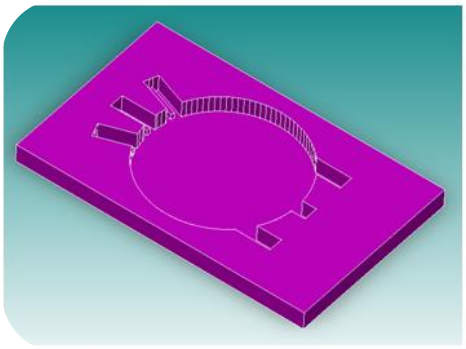

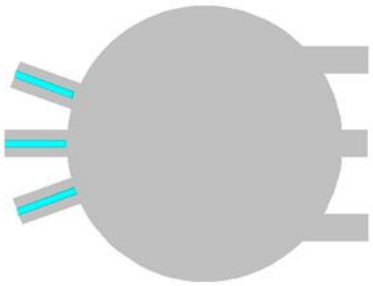

Mask 3

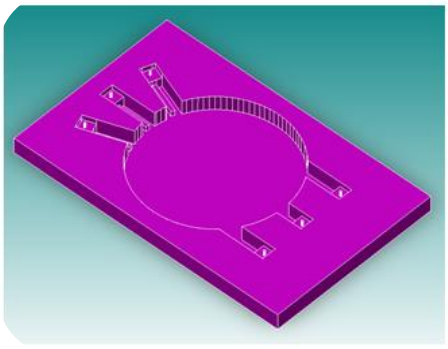

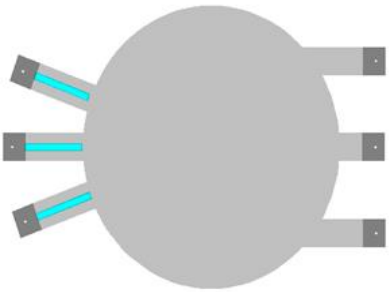

	Mask 4 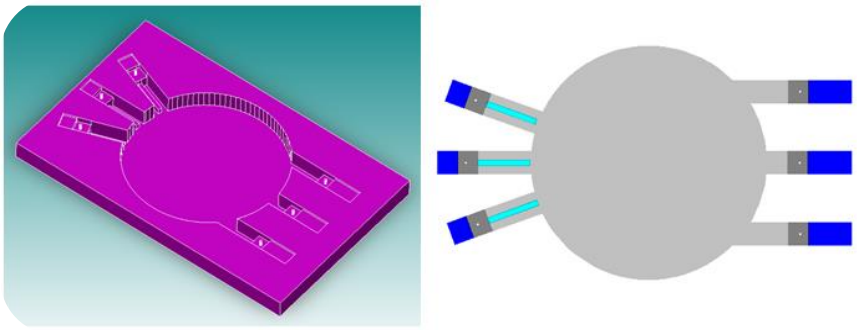			
2	Gold layer	G: LF	+ Cr + Au + Au	+ 50 nm + 50 nm + 1 µm
	Description: Cr is used as an adhesion layer for Au, but Ti, TiW, etc., can also be used. The thin 50nm Au is used as a seed layer for the electroplated thick Au on top. The last step in preparation of the bottom wafer is to cover the surface of the micromachined structures with a conducting material. Gold is selected as the coating material due to its unique characteristics of high conductivity, resistance to oxidation, and compatibility with the thermo compression bonding process. 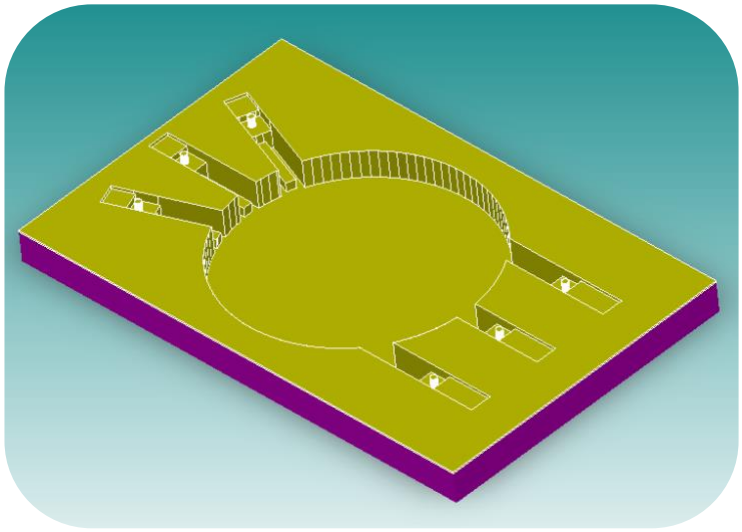			
#1: main step index, LF: light field, DF: dark field				

The top silicon wafer can be thinner because it is basically a top cover for the waveguide-based structures. Also, it has all the CPW/microstrip input/output planar lines. The figures describe in detail the process proposed to fabricate the top wafer.

Table 4-2 Main Microfabrication Steps of the Top Silicon Wafer

#1	Step	Mask	Material	Thickness
0	Cleaning of wafers	N.A.	N.A.	N.A.
	Description: The wafers are 2.5" square SVM silicon substrates with a relative permittivity of 11.68 and a loss tangent in the range of 10-4.			
1	Membrane deposition	M: LF	SiO2/Si3N4/SiO2	1 µm
	Description: A stacked layer of LPCVD SiO2/Si3N4/SiO2 membrane is deposited. This three-layer membrane is chosen to minimize stress so that the membrane does not buckle after the top silicon is removed. 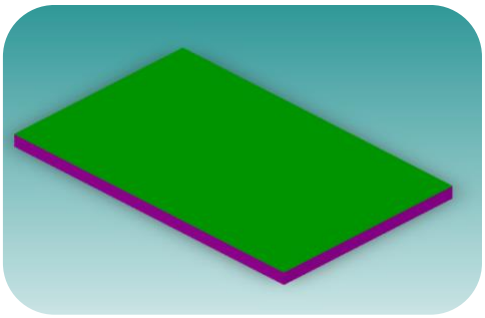			
2	Gold layer	G: LF	+ Cr + Au + Au	+ 50 nm + 50 nm + 1 µm
	Description: Cr is used as an adhesion layer for Au, but Ti, TiW, etc., can also be used. Gold is selected as the coating material due to its unique characteristics of high conductivity, resistance to oxidation, and compatibility with the thermo-compression bonding process.			

<table>
<tr><td></td><td colspan="4"> 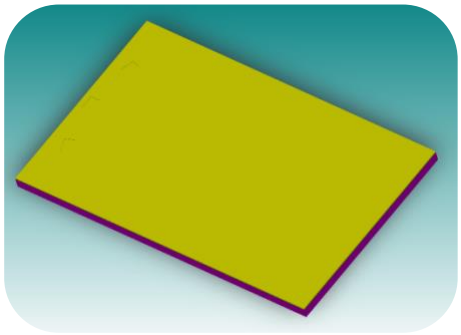 </td></tr>
<tr><td rowspan="2">3</td><td>Front etching</td><td>FE</td><td></td><td></td></tr>
<tr><td colspan="4">Description:
Front-etching is used to create the top wafer side that would cover the bottom wafer.
The CPW pads, the patch antenna, and via holes for the biasing of the PolymMUMPS switch are considered.
 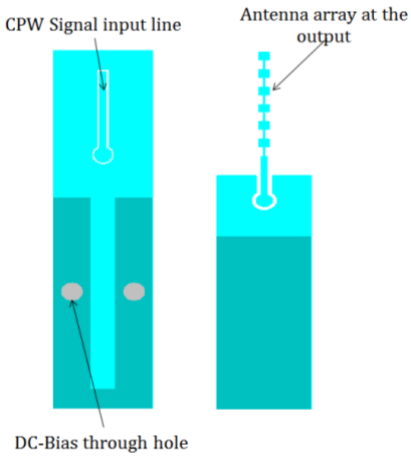
</td></tr>
<tr><td rowspan="2">4</td><td>Back etching</td><td></td><td></td><td></td></tr>
<tr><td colspan="4">Description:
Back-etching is used to access the CPW pads and also to suspend the antenna array only on the membrane to maximize radiation efficiency</td></tr>
<tr><td colspan="5">#1: main step index, LF: light field, DF: dark field, PI: polyimide</td></tr>
</table>

Once we finish fabricating both wafers, the bottom and top wafers are aligned and bonded using Au-Au thermo-compression bonding to form the completed structures (Figure 4-5). This process ensures continuity of the current flow between the top and bottom surfaces of the waveguides and structures. The bonding is performed under approximately 2000 kPa pressure and at a temperature of 380˚C for 40 minutes. The quality of the bonding between the surfaces is visually inspected by checking the cross-section of diced waveguide sections.

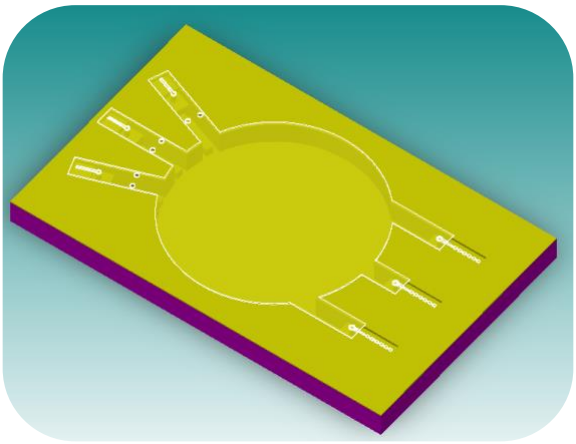

Figure 4-5 Bonding of top and bottom wafer

4.2.3 Micromachined 3D MEMS-Waveguide Design Stage 2: Folded Patch Antenna Array

In this section, we introduce a more compact design utilizing silicon via (TSV) to integrate the antenna on the back of the top wafer.

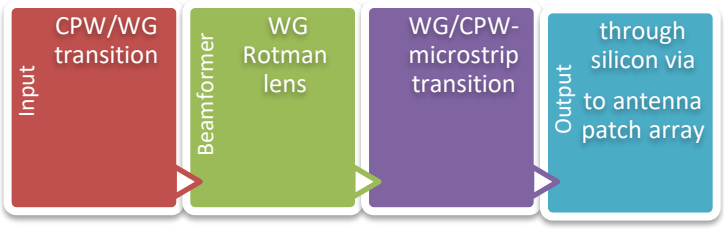

Figure 4-6 Top level presentation of the proposed stage 2

Therefore, nearly all of the same steps are used, except for patterning the antenna at the back of the wafer (Figure 4-6) and creating silicon via holes to connect the antenna to the classical transition. Table 4.3 summarizes the steps.

Table 4-3 Main Microfabrication Steps of the Top Silicon Wafer for Stage 2 Design

#1	Step	Mask	Material	Thickness
0	Cleaning of wafers	N.A.	N.A.	N.A.
	Description: The wafers are 2.5" square SVM silicon substrates with a relative permittivity of 11.68 and loss tangent in the range of 10-4.			
1	Membrane deposition	M: LF	SiO2/Si3N4/SiO2	1 µm
	Description: A stacked layer of LPCVD SiO2/Si3N4/SiO2 membrane is deposited. This three-layer membrane is chosen to minimize stress so that the membrane does not buckle after the top silicon is removed.			
2	Gold layer	G: LF	+ Cr + Au + Au	+ 50 nm + 50 nm + 1 µm
	Description: Gold is deposited on both sides of the silicon wafer.			
3	Front etching	FE		
	Description: Front-etching is used to create the top wafer side that will cover the bottom wafer. The CPW pads, the patch antenna, and via holes for the biasing of the PolymMUMPS switch are considered. The antenna patch array is not in this side of the wafer.			
4	Back etching			
	Description: Antenna patch array is defined and connected through silicon vias (TSV). Back-etching is used to access the CPW pads and also to suspend the antenna array on the membrane only to maximize radiation efficiency.			
#1: main step index, LF: light field, DF: dark field, PI: polyimide				

4.3 PolyMUMPS Actuator Simulation and Fabrication

Based on the switches presented in section 2.4, we simulated the mechanical behavior of the PolyMUMPS actuator with Comsol 4.3. The actuator is composed of a plate attached to an even number of legs from each side. The graph below presents the mechanical displacement for ten legs. We notice that by increasing the number of legs, the displacement of the plate is greater.

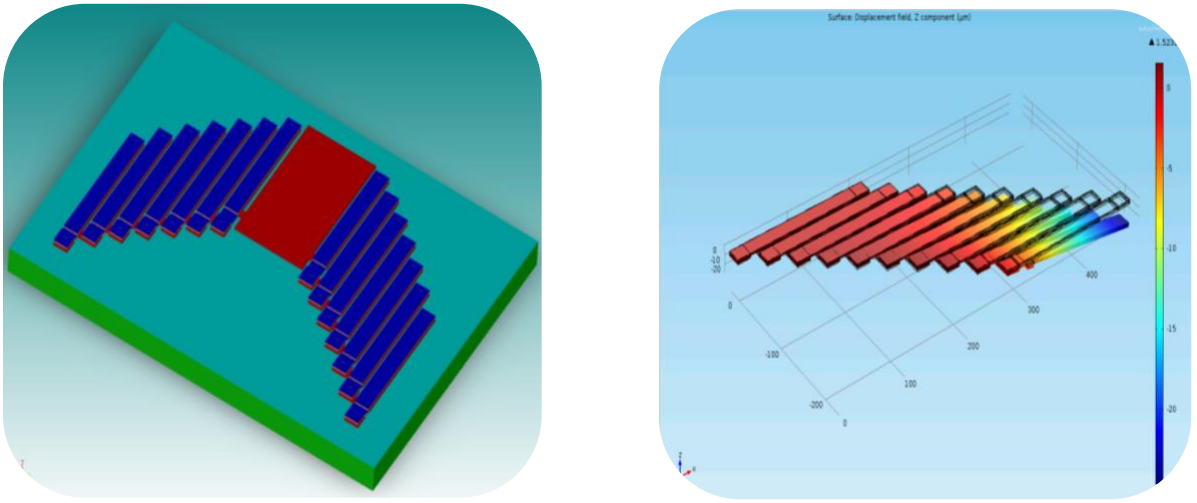

Figure 4-7 Proposed Actuator simulation

An SEM picture of the fabricated and released actuator is shown below:

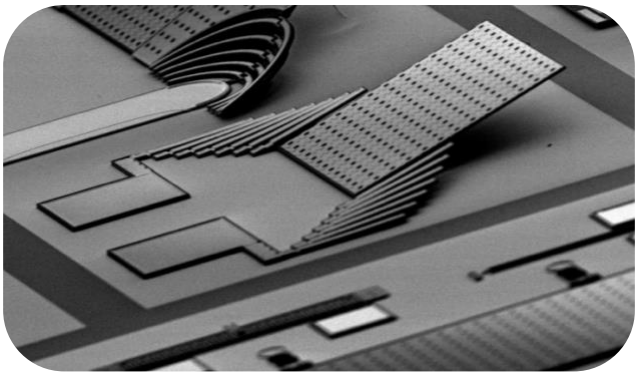

Figure 4-8 SEM picture of the PolyMUMPS actuator

Chapter 5
Conclusion

The 77 GHz band automotive radar has potentially better performance, smaller size and lower cost than the old 24 GHz band radar. However, the development of some key components, especially 77 GHz beam steering units, is still insufficient. RF MEMS (radio-frequency micro-electromechanical systems) technology allows for highly integrated, high-volume and low-cost components with superior RF performance. The benefits of RF MEMS are especially evident at frequencies in the mm-band as the dimensions of the structures shrink. In fact, standard machining methods are no longer suitable because of low fabrication tolerances and high cost of assembly. However, the structures show a very great degree of fabrication complexity due to errors in alignment, air gaps between conductive parts, poor metal contact, and inaccuracy in patterning that arise from non-contact lithography, complex assemblies of various parts, and the large number of steps needed for construction. It is envisioned that RF MEMS is a potential enabling technology for increasing the performance and reducing the costs of beam-steering units for future automotive radar.

As investigated in Chapters 3 and 4, different architectures would permit the integration of the front-end radar system in a single chip: A surface micromachined integrated BFN consisting of 77 GHz MEMS switches, a microstrip RL and an antenna array on a single substrate or a 3D MEMS-Waveguide micromachined single silicon substrate.

Bibliography

[1] Kim, Sang Gyu. Wideband two-dimensional and multiple beam phased arrays and microwave applications using piezoelectric transducers. *Diss. Texas A&M University*, 2005.

[2] Oberhammer, J., N. Somjit, U. Shah, and Z. Baghchehsaraei. RF MEMS for automotive radar sensors, *MEMS for automotive and aerospace applications*, 2013.

[3] Jlassi, Bahaedinne, Vahe Nerguizian, and Adel Merdassi. Design methodology of a high power RF MEMS switch for wireless applications, *2011 4th Annual Caneus Fly by Wireless Workshop*, 2011.

[4] Jain, Vipul. Millimeter-wave silicon-based ultrawideband automotive radar transceivers, 2011.

[5] Daneshmand, Mojgan. Multi-port RF MEMS switches and switch matrices, *Diss. University of Waterloo*, 2011.

[6] Vahidpour, M., M. Moallem, J. East, K. Sarabandi, M. Saif Islam, and Achyut Dutta. Micromachined lowmass RF front-end for beam steering radar, *Micro and Nanotechnology Sensors Systems and Applications IV*, 2012.

[7] Hamieh, Ismail. A 77 GHz Reconfigurable Micromachined Microstrip Antenna Array, *Diss. Windsor University*. 2013.

[8] Murad, M., J. Nickolaou, G. Raz, J. S. Colburn, and K. Geary. Next generation short range radar (SRR) for automotive applications, *2012 IEEE Radar Conference*, 2012.

[9] Oberhammer, J., N. Somjit, U. Shah, and Z. Baghchehsaraei. RF MEMS for automotive radar, *Handbook of MEMS for wireless and mobile applications*, 2013.

[10] Chen, Wan, Jiahui Fu, Qun Wu, and Jun Hua. A design of Rotman lens for phase antenna array, *2012 Asia-Pacific Symposium on Electromagnetic Compatibility*, 2012.

[11] Sinjari, A. MEMS based radar sensor for automotive collision avoidance, *Diss. Windsor University*, 2012.

[12] Bozzi, Maurizio, et al. Current and future research trends in substrate integrated waveguide technology. *Radioengineering 201-209*, 2009.

[13] Schoebel, Joerg, and Pablo Herrero. Planar Antenna Technology for mm-Wave Automotive Radar, Sensing, and Communications, *Radar Technology*, 2010.

[14] Sazzadur Chowdhury. Design of a PZT-based MEMS Rotman lens, *2008 Canadian Conference on Electrical and Computer Engineering*, 2008.

[15] Webber, Chris, and Hakan Gustafsson. Advanced Safety Systems—The Opportunity for Semiconductor Vendors. *Advanced Microsystems for Automotive Applications 2008. Springer Berlin Heidelberg*, 2008.

[16] Schulwitz, Lora Sue. Broadband millimeter-wave phased array circuits and antennas for polarimetric radar applications, *Diss, University of Michigan*, 2011.

[17] Ta, Hai Hoang. Compact RF/microwave passive components and modules on multilayer organic substrates. *University Of California, Davis*, 2012.

[18] Web. 15 Jan. 2014 **http://www.remcom.com/rotman-lens-designer**

[19] Baghchehsaraei, Zargham, Umer Shah, Jan Åberg, Göran Stemme, and Joachim Oberhammer. MEMS reconfigurable millimeter-wave surface for V-band rectangular-waveguide switch, *International journal of Microwave and Wireless Technologies*, 2013.

[20] Rahman, Hamood Ur, Jafar Babaei, Rodica Ramer, Jung-Chih Chiao, Lorenzo Faraone, Chennupati Jagadish, Jim Williams, and Alan R. Wilson. RF MEMS switches: design and performance in wireless applications, *Device and Process Technologies for Microelectronics MEMS Photonics and Nanotechnology IV*, 2007.

[21] Combrink, Carel J., Chris J. Venter, Seshan Govender, and Mohammed A. Alshareef. Reconfigurable, XML-driven, framework for real-time control and monitoring of embedded Radar Signal Processor, *2011 Saudi International Electronics Communications and Photonics Conference (SIECPC)*, 2011.

[22] Rebeiz, Gabriel M., et al. Mechanical modeling of MEMS devices: Static analysis. *RF MEMS: Theory, Design, and Technology*: 21-57, 2003.

[23] Web. 1 Nov. 2014. **http://www.triquint.com**.

[24] K. Shirahata. Radar sensor for automobiles, *1974 IEEE International Solid-State Circuits Conference Digest of Technical Papers*, 1974.

[25] M. ESASHI. Low Actuation Voltage Capacitive Shunt RF-MEMS Switch Having a Corrugated Bridge, *IEICE Transactions on Electronics*, 2006.

[26] Kamal Sarabandi. Monopulse-Doppler Radar Front-End Concept for Automotive Applications Based on RF MEMS Technology, *2006 IEEE International Conference on Electro/Information Technology*, 2006.

[27] Vahidpour, Mehrnoosh. A Millimeter-Wave Radar Microfabrication Technique and Its Application in Detection of Concealed Objects. *Diss. University of Michigan*, 2012.

[28] D. Chicherin. Analog type millimeter wave phase shifters based on mems tunable high-impedance surface in rectangular metal waveguide, *2010 IEEE MTT-S International Microwave Symposium*, 2010.

[29] Zhiping Feng. Narrowband Barium Strontium Titanate (BST) tunable bandpass filters at X-band, *2009 IEEE MTT-S International Microwave Symposium Digest*, 2009.

[30] Kin-Lu Wong. Experimental study of a two-element dual-frequency microstrip array, *Microwave and Optical Technology Letters*, 1997.

[31] W. Rotman. Wide-angle microwave lens for line source applications, *IEEE Transactions on Antennas and Propagation*, 1963.

[32] Lal, Sundeep. An FPGA-based 77 GHzs RADAR Signal Processing System for Automotive Collision Avoidance, 2011.

[33] Morgan, Robert W. A new paradigm in optimal missile guidance, *Diss, University of Arizona*, 2011.

[34] S. Dhar. Radar target modeling and 2D ISAR imaging at 76GHz for ITS application, *2011 Annual IEEE India Conference*, 2011.

[35] E. Ragonese. A 0.13m SiGe BiCMOS LNA for 24-GHz Automotive Short-Range Radar, *2008 38th European Microwave Conference*, 2008.

[36] Wang, Minfeng. Fabrication and Characterization of MEMS Direct-Contact Switches in Laminates. *University of California, Irvine*, 2012.

[37] Gokul, K. C.; Gurung, D. B. and Adhikary, P. R. Modeling airflow effects in human eye temperature with and without eyelids, *International Journal of Applied Mathematics & Mechanics*, 2014.

[38] Khraisat, Yahya S. H. Simulation of the 24GHz Short Range, Automotive Radar, *European Journal of Scientific Research*, 2011.

[39] Mahafza. Doppler Processing, *Radar Signal Analysis and Processing Using MATLAB*, 2008.

[40] Sterner, Mikael, and Joachim Oberhammer. Symmetrical Antidirectional Metallization for Stress Compensation of Transfer-Bonded Monocrystalline Silicon Membranes, *Journal of Microelectromechanical Systems*, 2012.

[41] Zhang, Zhenyu. Substrate Integrated Waveguide Devices and Receiver Systems for Millimeter-Wave Applications. *Diss. École Polytechnique de Montréal*, 2011.

[42] Cetintepe, Cagri, Ebru Sagiroglu Topalli, Simsek Demir, Ozlem Aydin Civi, and Tayfun Akin. A fabrication process based on structural layer formation using Au–Au thermocompression bonding for RF MEMS capacitive switches and their performance, *International Journal of Microwave and Wireless Technologies*, 2014.

[43] Malmqvist, Robert, Aziz Ouacha, Mehmet Kaynak, Naveed Ahsan, and Joachim Oberhammer. Reconfigurable RF Circuits and RF-MEMS, *Microwave and Millimeter Wave Circuits and Systems Emerging Design Technologies and Applications*, 2012.

[44] R. Sorrentino. Real-time interference nulling method T1A.3 for mobile communication systems *Proceedings 2004 IEEE Radio and Wireless Conference*, 2004

[45] I. Gresham. Ultra-Wideband Radar Sensors for Short-Range Vehicular Applications, *IEEE Transactions on Microwave Theory and Techniques*, 2004.

[46] Kagan Topalli. A Monolithic Phased Array Using 3-bit Distributed RF MEMS Phase Shifters, *IEEE Transactions on Microwave Theory and Techniques*, 2008.

[47] Gabriel M. Rebeiz. Introduction: RF MEMS for Microwave Applications, *RF MEMS*, 2003

[48] Ke Wu, , Yu Jian Cheng, T. Djerafi, and Wei Hong. Substrate-Integrated Millimeter-Wave and Terahertz Antenna Technology, *Proceedings of the IEEE*, 2012.

[49] Abhulimen, Isibhakhomen Umolu. Characterization of Deep Reactive Ion Etching (DRIE) for Via Formation in Chip Stacking Applications. *ProQuest*, 2008.

[50] Vahidpour, Mehrnoosh, and Kamal Sarabandi. 2.5D Micromachined 240 GHz Cavity-Backed Coplanar Waveguide to Rectangular Waveguide Transition, *IEEE Transactions on Terahertz Science and Technology*, 2012.

[51] Ozkeskin, Fatih. Bulk Foil Platinum-Rhodium Micro-relays for High Power RF and Other Applications, *Diss. University of Michigan*, 2012.

[52] Alexeenko, A.. Uncertainty in microscale gas damping: Implications on dynamics of capacitive MEMS switches, *Reliability Engineering and System Safety*, 2011.

[53] Wang, Yu Albert. RF MEMS switches and phase shifters for three-dimensional MMIC phased array antenna systems, *Diss. University of Hong Kong*. 2011.

[54] Web. 9 Oct. 2014. **https://uwaterloo.ca/centre-integrated-rfengineering/sites/ca.centre-integrated-rf-engineering/files/uploads/files /uwmems_design_handbook_5.0_0.pdf**.

[55] AS Abdellatif, N Ranjkesh, M Fahimnia, A Taeb, S Gigoyan ,Low insertion loss variable phase shifter for emerging millimeter-wave communication systems, *Microwave Symposium (IMS)*, 2014 IEEE MTT-S International, 1-4. 2014

[56] Web. 9 Oct. 2014. **https://freescale.com**

[57] Web. 9 Oct. 2014. **https://infineon.com**

[58] Web. 9 Oct. 2014. **https://npx.com**

[59] UW-MEMS handbook version 4.0 .9 Oct. 2014. **https://uwaterloo.ca/centre-integrated-rf-engineering/**